On the Singular Nature of the Second-Order Peaks in HF Radar Sea Echo

Dmitry V. Ivonin, Victor I. Shrira, and Pierre Broche

***Abstract*—Electromagnetic (EM) scattering from the sea surface concerned with second-order Doppler spectra for finite-length pulses is theoretically analyzed in the scattering regime typical of, but not confined to, high-frequency (HF) radars. The Doppler spectra of the second-order cross section consist of three different parts: continuum and two pairs of peaks—the *second harmonic* and *corner reflection peaks*. This paper is the first investigation of fundamental properties of these peaks from the perspective of their use in measurements of surface currents. It is shown that these peaks are of singular nature in the following sense: The main (singular) contribution is due to particular pairs of waves, despite the fact that waves of many different wavelengths and directions contribute to these peaks. This fact opens a possibility to employ these peaks in remote sensing of vertical profiles of surface currents. Using the number of waves in the pulse ("the pulse length") $L \gg 1$ as a large parameter, an asymptotic description of these peaks is developed. Height, width, and position of the peaks are explicitly found in terms of L. The peak positions, to the leading order, do not depend on the pulse length, although a small explicitly found $O(L^{-1})$ shift has to be taken into account for the corner reflection peaks. The heights are $\sim \ln L$ and $\sim L^{1/2}$ for the second harmonic and corner reflection peaks, respectively. The results open the way for wider use of the second-order peaks for probing surface currents.**

***Index Terms*—Corner reflection peak, electromagnetic (EM) scattering from sea surface, pulsed high-frequency (HF) radars, remote sensing of currents, second harmonic peak, vertical shear.**

I. Introduction

HIGH-FREQUENCY (HF) radar devices are strengthening their position as indispensable tools in monitoring of the sea surface. In particular, the sea-echo Doppler spectra of HF radars are routinely used for measurements of sea waveheights and surface currents, while the search continues for ways of remote sensing of other aspects of air–sea interaction (e.g., [1]–[3]). The theoretical framework, upon which the use of HF radars is based, was developed more than three decades ago and is totally adequate for their present way of use. However, for finding novel ways of using the same devices, the questions rooted in theory have to be revisited and addressed. This paper investigates one such question prompted by the idea of tempting possibility of more "efficient" use of the existing devices.

Following the pioneering work by Crombie [4], who observed and identified the main features of sea-echo Doppler spectra, the theoretical foundations of HF remote sensing were laid down by Weber and Barrick [5], [6] and Lipa and Barrick [7], where a systematic asymptotic weakly nonlinear theoretical formulation has been developed. In particular, it describes the HF sea-echo Doppler spectrum due to an incident monochromatic wave in terms of the ocean wave spectrum and the surface current velocity [8]. Walsh and Gill [10] systematized and extended Barrick's results to bistatic applications and to finite length of the emitted electromagnetic (EM) pulse.

The resulting understanding of the observed sea echoes is that the first-order Doppler spectrum explains the two highest peaks in the spectrum as manifestations of Bragg scattering and that the second-order Doppler spectrum describes the surrounding continuum and the two pairs of smaller peaks, called the *second harmonic* peaks and the *corner reflection* peaks, respectively. Since the first-order peaks result from scattering by surface gravity waves of specific wavelength and direction (the Bragg waves), it is straightforward to estimate velocity of surface current employing the known dispersion relation. The discrepancy between the observed frequency of the Bragg lines and the linear dispersion relation for resonant surface gravity waves is attributed to the Doppler shift of the frequency of resonant waves due to the presence of surface shear current. The shift is proportional to an integral over depth of the surface current with an exponential weighting function specified by the radar frequency. Thus, the prevailing way of using HF radars for measurements of surface currents enables one to measure just a certain depth averaged current: an integral with a specific weighting function.

The possibility to utilize also the second-order (*second harmonic* and *corner reflection*) peaks for measuring the current velocity in a similar manner hinges on whether these second-order peaks can be deterministically linked to some *particular* combinations of wave Fourier components. If the answer is positive, then, since the corresponding Doppler shifts of these components depend both on their wave vectors and the vertical structure of the surface currents, these shifts could be used for remote sensing of the vertical structure of the surface currents. In the context of probing the currents, the second fundamental open question is whether there is no bias in the positions of these peaks. The questions are vital for use/nonuse of the peaks, and, therefore, are of true practical importance.

The second-order Doppler spectrum at each frequency is a result of contributions of a continuum of waves of different lengths

Manuscript received May 23, 2005; accepted September 1, 2006. The work was supported in part by INTAS Junior Scientist Fellowship under Contract 181/01, International Association for Promotion of Cooperation with Scientists from New Independent States of the Former Soviet Union (INTAS) 97-575, 01-234, Russian Foundation for Basic Research under Grant N01-05-64603-a, and Russian Science Support Fund. **Associate Editor: M. L. Heron**.

D. V. Ivonin is with the Shirshov Institute for Oceanology, Russian Academy of Sciences, Moscow 117851, Russia (e-mail: dima@wave.sio.rssi.ru).

V. I. Shrira is with the Department of Mathematics, Keele University, Keele ST5 5BG, U.K. (e-mail: v.i.shrira@keele.ac.uk).

P. Broche is with Laboratoire de Sondages Electromagnétiques de l'Environnement Terrestre (LSEET), Université de Toulon et du Var, La Garde 83957, France (e-mail: broche@lseet.univ-tln.fr).

Digital Object Identifier 10.1109/JOE.2006.886080

and directions. At the face of it, this fact excludes a possibility to link the second-order peaks to specific wave numbers. However, and this is the main point of this paper, we show that the contributions of *particular* wave components to the second-order Doppler spectrum are singular, i.e., their contributions to the echo far exceed those due to other waves. More specifically, we show that the second harmonic peaks are primarily due to the second harmonic of the water wave of wavelength twice that of the Bragg wave and propagating parallel to the radar beam, while the corner reflection peaks are due to a pair of oblique waves propagating at angles $\pm\pi/4$ to the radar beam and having the length equal to that of the square root of twice the Bragg resonant wave.

Moreover, we also demonstrate that the bias of their positions due to the slope of the continuum is small: It is either negligible (as for the second harmonic peaks) or easily taken into account via a simple explicit formula (as it is the case for the corner reflection peaks). Thus, indeed, the second-order peaks can be used for measurements of the vertical structure of surface currents, which has been recently confirmed experimentally by Shrira *et al.* [11] and Ivonin *et al.* [12]. The additional information provided by the second-order peaks enables one to find two extra integrals of surface current with different weighting functions, which allows one to estimate the current vertical profile.

Although the elucidation of the nature of these peaks is the central point of this paper, the bulk of the paper is concerned with development of their analytical description for the situation of pulsed incident EM wave. The analytical description of the peaks is needed to facilitate developments of more efficient signal processing techniques which in the long run would allow one to discern the peaks in the field data under less favorable signal-to-noise ratio (SNR) conditions than is common today.

The work is organized as follows. In Section II, we give the mathematical formulation of the problem. In Section III, the integrals are evaluated asymptotically, making use of L as a large parameter, and explicit analytical expressions for the peak parameters are presented. In Section IV, we summarize the results and discuss the perspectives, context, and open questions. The details of the derivation are given in Appendices A–C.

II. Second-Order Cross Section

A. Classical Picture and Its Shortcomings

A typical radar echo spectrum in the HF or very high-frequency (VHF) range consists of a continuum and a number of peaks imbedded into it, as illustrated in Fig. 1. Such spectra are well understood and first we highlight the main points of the established picture. The two highest peaks of the spectrum are due to the first-order scattering by the "Bragg waves": resonantly selected specific spectral components of the wind wave field, which for typical HF radar applications at low-grazing angles have the wavelength close to one-half the radar wavelength. These waves can move both towards and away from the radar; in the absence of currents, the peaks are located at $\pm f_B$, where $f_B = \sqrt{2gk_0}/(2\pi)$ is the frequency of "Bragg waves" in hertz (g is the gravitational acceleration and k_0 is the radar wave number). The presence of currents shifts the positions of the peaks proportionally to the projection of the current on the corresponding direction and, hence, creates a straightforward way of measuring the currents, since their heights are two orders of magnitude greater than the heights of surrounding continuum and other peaks.

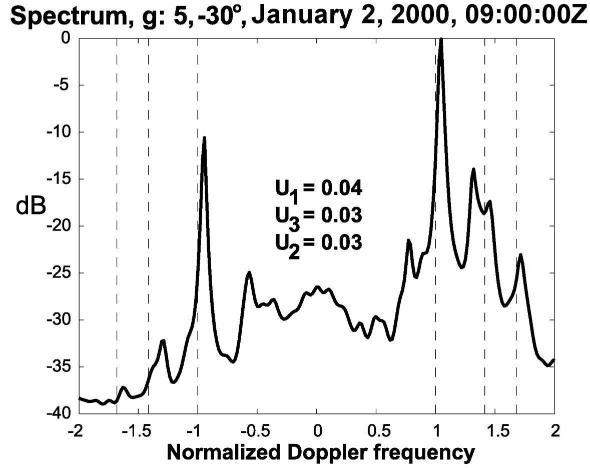

Fig. 1. Example of typical sea-echo power spectrum. The frequency axis is in units of the Bragg frequency $f_B = \sqrt{2gk_0}/(2\pi)$; the dashed vertical lines mark the unperturbed by currents positions of the first-order peaks at ± 1, the second harmonic peaks at $\pm\sqrt{2}$, and the corner reflection peaks at $\pm 2^{3/4}$. U_1, U_2, and U_3 are respective peak displacements (in f_B) due to the presence of the current.

The continuum and other peaks are primarily due to second-order scattering, which can be viewed as a result of the summation over all "elementary" consequent scatterings from two wave systems with wave vectors $\mathbf{k}_1$ and $\mathbf{k}_2$, satisfying the Bragg resonance condition

$$\mathbf{k}_1 + \mathbf{k}_2 = \pm\mathbf{k}_B \tag{1}$$

($\mathbf{k}_B \approx -2\mathbf{k}_0$ is the Bragg wave vector and $\mathbf{k}_0$ is the wave vector of the incident EM wave). The general solution automatically satisfying the resonance condition (1) is provided by a parametric representation of vectors $\mathbf{k}_{1,2}$ in terms of two scalars p and q (below, we will consider the case $\mathbf{k}_1 + \mathbf{k}_2 = \mathbf{k}_B$, since the case $\mathbf{k}_1 + \mathbf{k}_2 = -\mathbf{k}_B$ can be considered absolutely in a similar manner)

$$\mathbf{k}_0 = (k_0, 0) \quad \mathbf{k_1} = (p - k_0, q) \quad \mathbf{k}_2 = (-(p + k_0), -q) \tag{2}$$

where p is introduced to be parallel to the radar beam and directed against it, with q being perpendicular.

The Doppler frequency of backscattered echo unperturbed by currents is specified by the frequency-resonance condition (see Fig. 2)

$$\omega = \pm\sqrt{gk_1} \pm \sqrt{gk_2}. \tag{3}$$

For a monochromatic incident EM wave $e^{j\omega_0 t}$, the Doppler spectrum of the second-order cross section $\sigma^{(2)}(\omega)$ is given by Barrick's equation [6]

$$\sigma^{(2)}(\omega) = 2^6\pi k_0^4 \sum_{l_1=\pm 1}\sum_{l_2=\pm 1}\int\int |\hat{\Gamma}|^2 S(\mathbf{k_1})S(\mathbf{k_2}) \cdot \delta(\omega - l_1\sqrt{gk_1} - l_2\sqrt{gk_2})\, dp\, dq \tag{4}$$

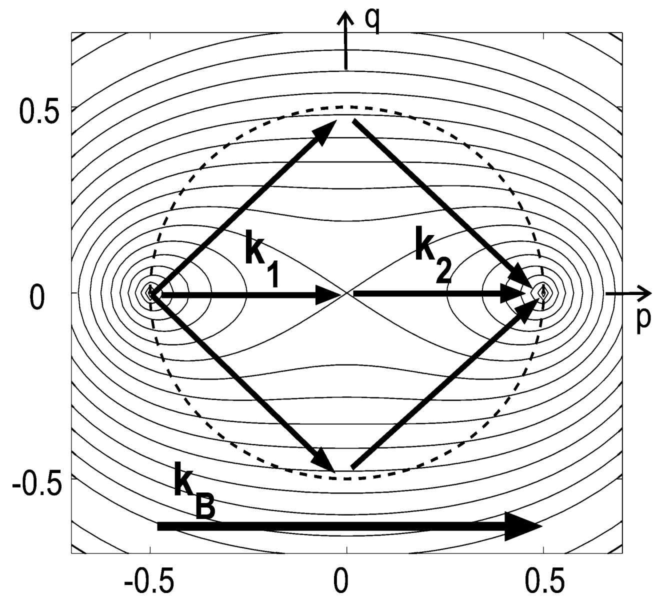

Fig. 2. Contours of constant Doppler frequency ω versus wave numbers p and q (the p-axis is against the beam direction), for a pair of water wave vectors $\mathbf{k_1}$ and $\mathbf{k_2}$ producing second-order backscattering, for $|\omega| > \omega_B$. The contours of constant ω for $\mathbf{k_1}$ and $\mathbf{k_2}$ satisfying (1) are specified by (3) and shown in thin lines. The horizontal bold arrow at the bottom represents the Bragg wave vector. The dashed curve indicates the EM "corner reflection" condition, where $\mathbf{k_1}$ and $\mathbf{k_2}$ are perpendicular and satisfy condition (1). Bold arrows show the combination of $\mathbf{k_1}$ and $\mathbf{k_2}$: i) for the singular situation at $|\omega| = 2^{1/2}\omega_B$ in (4), where the two closed contours break apart; and ii) the combination $\mathbf{k_1}$ and $\mathbf{k_2}$, where the "corner reflection" circle is tangent to the Doppler frequency contour $|\omega| = 2^{3/4}\omega_B$.

where $S(\mathbf{k})$ is the wave energy spectrum, $k_0 = |\mathbf{k_0}|$ is the Bragg wave number, and $\hat{\Gamma} = \hat{\Gamma}_H + \hat{\Gamma}_{\mathrm{EM}}$ is the coupling coefficient. Here, $\hat{\Gamma}_H$ and $\hat{\Gamma}_{\mathrm{EM}}$ are the hydrodynamic and EM components given by

$$\hat{\Gamma}_H = \frac{-i}{2}\left[k_1 + k_2 - \frac{(k_1k_2 - \mathbf{k_1}\cdot\mathbf{k_2})(\omega^2+\omega_B^2)}{l_1l_2\sqrt{k_1k_2}(\omega^2-\omega_B^2)}\right]$$
$$\hat{\Gamma}_{\mathrm{EM}} = \frac{1}{2}\left[\frac{\dfrac{(\mathbf{k_1}\cdot\mathbf{k_0})(\mathbf{k_2}\cdot\mathbf{k_0})}{k_0^2} - 2\mathbf{k_1}\cdot\mathbf{k_2}}{\sqrt{\mathbf{k_1}\cdot\mathbf{k_2}} - k_0\Delta_w}\right]$$

where $\omega_B = \sqrt{gk_B}$ is the Bragg frequency in radians per second, and Δ_w is the average normalized impedance at the interface [7]. Throughout the paper, we will assume $\Delta_w \approx 0.011 - i0.012$, which is a typical value of the impedance for a rough sea [9].

The constraints imposed by the resonance conditions (1) and delta function in (3) specify contours of integration in the (p, q) plane (see Fig. 2), which determine all possible pairs of $\mathbf{k_1}$ and $\mathbf{k_2}$ contributing to second-order scattering at any fixed Doppler frequency $\omega = \mathrm{const}$. The contours are the so-called Phillips' eights [13]. It is easy to see that many (continuum of) combinations of water waves of different lengths and directions contribute to the second-order scattering at the same Doppler frequency (see also Fig. 2). Hence, the responses of many different waves are mixed in the second-order echo and, *a priori*, it seems impossible to distinguish a contribution due to any particular spectral component.

Barrick's formula (4) describes the behavior of the second-order continuum and *positions* of the secondary peaks reasonably well. However, it fails (see Section II-B) to describe them quantitatively because of a singularity of logarithmic type at the second harmonic peak and gives wrong results for the corner reflection peak. Of course, the second-order cross section could not have a singularity. The divergence of the second-order term in the asymptotic expansion by Weber and Barrick [5] just implies that to obtain a regular solution, a different expansion employing fractional powers of the small parameter (ratio of the waveheight to the wavelength) is needed near the second harmonic. However, such an expansion would be of limited interest, since in reality there are other factors which regularize the integral without a necessity to employ a more elaborate perturbation scheme. The main such factors are the finite spectral width of the impulse emitted by the radar and the finite aperture of the antennae, each of them independently leads to a finite cross section near $\omega = \sqrt{2}\omega_B$. We focus on investigating just the first factor, since it proves to be sufficient for answering the key questions we are interested in, while the effect of finite aperture could be treated in a similar manner.

B. Logarithmic Singularity

As we discussed previously, Barrick's integral (4) has a singularity at $|\omega| = \sqrt{2}\omega_B$ near the saddle point $p = q = 0$, where the integration contours break apart. Let us split the integral into two parts: 1) integration over an ϵ–vicinity of the origin ($\epsilon \ll 1$); and 2) integration over the rest of the plane

$$\sigma^{(o)} = \int\int_{p^2+q^2<\epsilon} \ldots\, dp\, dq$$
$$\sigma^{(r)} = \int\int_{p^2+q^2>\epsilon} \ldots\, dp\, dq. \tag{5}$$

Expanding the argument of the δ-function near the origin, we find for the integral $\sigma^{(o)}$

$$\sigma^{(o)} = \mathrm{Const}\int\int_{p^2+q^2<\epsilon} \delta(p^2 - 2q^2)\, dp\, dq.$$

The coordinate transformation

$$p - 2^{1/2}q = \xi \quad p + 2^{1/2}q = \zeta$$

and integration over ζ yields

$$\sigma^{(o)} = \mathrm{Const}\int_{-\epsilon}^{\epsilon}\int_{-\epsilon}^{\epsilon} \delta(\xi\,\zeta)\, d\xi\, d\zeta = \mathrm{Const}\int_{-\epsilon}^{\epsilon} \frac{d\xi}{\xi}.$$

The integral $\sigma^{(o)}$ diverges because of a *nonintegrable* singularity of logarithmic type, while the integral over the rest of the plane, $\sigma^{(r)}$, is finite. The second harmonic peak appears entirely due to the neighborhood of the origin. Thus, $\sigma^{(o)}$ corresponds to the second harmonic peak, while $\sigma^{(r)}$ is naturally linked with the continuum. Roughly speaking, the former produces the peak, while the latter yields the base of the peak. In reality, the peak is finite as well as is the neighborhood which contributes to it. Later, we will obtain a generalization of Barrick's formula with the δ-function corresponding to an idealized monochromatic radio wave replaced by the "smeared δ-function" resulting from the finite-length radar pulse. The integration path contours prescribed by the δ-function are replaced by the strips of width specified by the nondimensional pulse length L (defined in Section II-C). The asymptotic analysis carried out later will provide the height, width of the peak, and the shift of its position due to continuum, all expressed in terms of the pulse length.

C. Finite Pulse Length

Following [10], assume the excitation current to be modelled as a pulsed sinusoid:

$$i(t) = I_R\, e^{j\,\omega_R t}[h(t) - h(t-\tau_R)]$$

where I_R is the peak current, ω_R is the operational radian frequency of the radar, τ_R is the pulse duration, and $h(t)$ is the Heaviside function. Then, the second-order cross section (we confine our attention to the monostatic case only) is expressed as

$$\begin{aligned}\sigma_2(\omega) = {} & 2^3\pi^2 k_0 L \sum_{l_1,l_2=\pm 1} \int_0^\infty \int_{-\pi}^{\pi} \int_0^\infty |\hat{\Gamma}|^2 \\ & \cdot S(l_1\mathbf{k}_1)\, S(l_2\mathbf{k}_2) \left[\frac{\sin\left(\pi L \left[\frac{k}{(2k_0)} - 1\right]\right)}{\left(\pi L \left[\frac{k}{(2k_0)} - 1\right]\right)} \right]^2 \\ & \cdot \delta\Big(\omega - l_1\sqrt{gk_1} - l_2\sqrt{gk_2}\Big)\, k^2\, k_1\, dk_1\, d\theta\, dk \end{aligned} \quad (6)$$

where the same notations as in (4) are kept and θ is the angle between the vectors $\mathbf{k}_1$ and $(p, 0)$ (Fig. 2). The parameter $L = \omega_R \tau_R / 2\pi$ is the number of Bragg waves in the "sea patch," or, equivalently, the number of radio waves in the radar pulse. Equation (6) derived by Walsh and Gill in [10] differs from Barrick's equation by an additional convolution with the square of the Dirichlet function, which we will denote as $s(\ldots)$

$$s(x) = \left[\frac{\sin(x)}{x}\right]^2. \quad (7)$$

The Dirichlet function is the Fourier transform of a rectangular radar pulse. The convolution with its square implies that the condition of the exact resonance type on the combination $\mathbf{k}_1 + \mathbf{k}_2$ disappears and is replaced by a somewhat milder condition. The global maximum of the kernel still corresponds to the Bragg resonance $\mathbf{k}_1 + \mathbf{k}_2 = \mathbf{k}_B$, while the other maxima correspond to the sidelobes $\mathbf{k}_1 + \mathbf{k}_2 = (1 + m/L)\,\mathbf{k}_B$, where $m = \pm(1, \infty)$.

The presence of the δ-function in the integral (6) suggests that one integration can be eliminated. Although the argument of the δ-function in (6) is unsuitable for a direct integration over k_1 or k_2, the following trick makes the integration possible. We introduce a scale factor ν relating k and k_B: $k = \nu^2 k_B$. Then, using the same factor, we introduce two new wave vectors $\hat{\mathbf{k}}_1$ and $\hat{\mathbf{k}}_2$ similarly linked to $\mathbf{k}_1$ and $\mathbf{k}_2$

$$\mathbf{k}_1 = \nu^2 \hat{\mathbf{k}}_1 \quad \mathbf{k}_2 = \nu^2 \hat{\mathbf{k}}_2 \quad (\mathbf{k} = \nu^2 \mathbf{k}_B).$$

As a result the integration over k in (6) can be replaced by integration over ν

$$\begin{aligned}\sigma_2(\omega) = {} & 2^7\pi^2 k_0^4 L \sum_{l_1,l_2=\pm 1} \int_0^\infty \hat{k}_1 d\hat{k}_1 \int_{-\pi}^{\pi} d\theta_{\hat{\mathbf{k}}_1} \int_0^\infty |\hat{\Gamma}|^2 \\ & \cdot S(l_1\nu^2\hat{\mathbf{k}}_1)\, S(l_2\nu^2\hat{\mathbf{k}}_2)\, s\left[\pi L\left(\nu^2 - 1\right)\right] \\ & \cdot \frac{\delta\left(\frac{\omega}{\left[l_1(g\hat{k}_1)^{1/2} + l_2(g\hat{k}_2)^{1/2}\right]} - \nu\right)}{\left[l_1(g\hat{k}_1)^{1/2} + l_2(g\hat{k}_2)^{1/2}\right]} \nu^9\, d\nu \end{aligned} \quad (8)$$

where we used the following relations:

$$\begin{aligned} & \delta\Big(\omega - l_1\,(gk_1)^{1/2} - l_2\,(gk_2)^{1/2}\Big) \\ & = \delta\left(\omega - \nu\left[l_1(g\hat{k}_1)^{1/2} + l_2(g\hat{k}_2)^{1/2}\right]\right) \\ & = \frac{\delta\left(\frac{\omega}{\left[l_1(g\hat{k}_1)^{1/2} + l_2(g\hat{k}_2)^{1/2}\right]} - \nu\right)}{\left[l_1(g\hat{k}_1)^{1/2} + l_2(g\hat{k}_2)^{1/2}\right]}. \end{aligned}$$

Then, the last integral reduces to a formula similar to Barrick's (we will omit the hats)

$$\begin{aligned}\sigma_2(\omega) = {} & 2^7\pi^2 k_0^4 \omega^{-1} L \sum_{l_1,l_2=\pm 1} \int_0^\infty \int_{-\pi}^{\pi} |\Gamma|^2\, S(l_1\chi\mathbf{k}_1) \\ & \cdot S(l_2\chi\mathbf{k}_2)\; s\left[\pi L\,(\chi - 1)\right]\, \chi^5\, k_1 dk_1\, d\theta_{\mathbf{k}_1} \end{aligned} \quad (9)$$

where a nondimensional scale factor χ, which appeared due to the δ-function constraint, is given by

$$\chi(k_1, k_2, \omega) \equiv \frac{\omega^2}{\left[l_1(gk_1)^{1/2} + l_2(gk_2)^{1/2}\right]^2}.$$

The squared Dirichlet function $s[\ldots]$ replaces here the δ-function of Barrick's integral; it acts as a smeared delta function and prescribes the integration along strips instead of contours (cf. Figs. 2 and 3). The assumed large parameter L, the number of Bragg waves inside the sea patch, determines also the strip width which obviously decreases with L. The general behavior of $s[\ldots]$ and the shape of the integration domain at $\omega = \sqrt{2}\omega_B$ (confined in the chosen example by isolines $s[\pi L(\chi - 1)] = 0.1$) are illustrated for $L = 200$ in Fig. 3. This domain consists of a spot of width $\sim L^{-1/2}$ and two strips of width $\sim L^{-1}$.

Now, we can indeed split the integration domain into two ($\sigma_2^{(o)}$ and $\sigma_2^{(r)}$) and proceed with the detailed analysis of the integral which took the form similar to Barrick's formula (4) with the only difference that the δ-function is replaced by the squared Dirichlet function (7).

III. Evaluation of the Cross-Section Integral

A. Simplification of Basic Formulas

In this section, starting with the modified Barrick's formula (9), we deduce explicit analytic formulas for the continuum, the

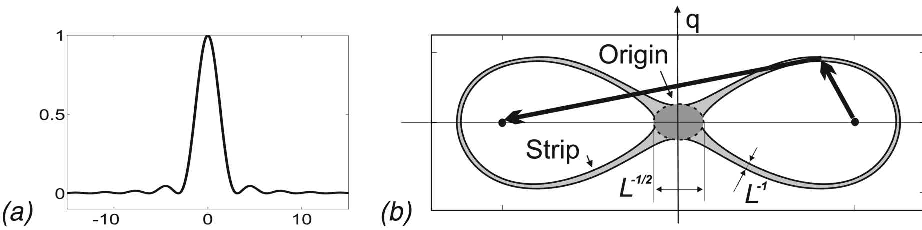

Fig. 3. (a) Square of the Dirichlet function $s(x)$. (b) Integration domain (the strips) at $\eta = 2^{1/2}$ prescribed by the function $s[\pi L(\chi - 1)]$ for $L = 200$. The plotted domain is confined by the condition $s > 0.1$. The light gray region is the $O(L^{-1})$ strip where integral (4) is valid. The dark gray spot of width $O(L^{-1/2})$ near the origin indicates the saddle-point domain, where special consideration is required.

second-order peak, and the corner reflection peak. We will consider the domain $\omega > \omega_B$ only, which corresponds to the choice $l_1 = l_2 = 1$; hence, the indexes l_1 and l_2 will be omitted. The case $\omega < -\omega_B$ with $l_1 = l_2 = -1$ is treated similarly.

We will use for calculations a more convenient normalized representation of the modified Barrick's formula (9), the same as in [7]. In particular, for wave vectors

$$\mathbf{K}_1 = \frac{\mathbf{k}_1}{(2k_o)} \quad \mathbf{K}_2 = \frac{\mathbf{k}_2}{(2k_o)} \quad K_1 = |\mathbf{K}_1| \quad K_2 = |\mathbf{K}_2|.$$

Correspondingly

$$\tilde{p} = \frac{p}{(2k_o)} \quad \tilde{q} = \frac{q}{(2k_o)}$$

and

$$K_1 = \left(\tilde{p} - \frac{1}{2}, \tilde{q}\right) \quad K_2 = \left(-\tilde{p} - \frac{1}{2}, -\tilde{q}\right).$$

Frequencies are normalized by the Bragg frequency $\Omega = \omega/\omega_B$, while the coupling coefficient by the Bragg wave number $\tilde{\Gamma} = \hat{\Gamma}/(2k_o)$. The wind wave spatial spectrum and the scale factor χ become

$$\tilde{S}(\mathbf{K}) = (2k_o)^4\, S(\mathbf{k}), \tilde{\chi}(K_1, \theta, \Omega) = \frac{\Omega^2}{(\sqrt{K_1} + \sqrt{K_2})^2}$$

where

$$K_2 = \left(K_1^2 + 2K_1 \cos\theta + 1\right)^{1/2}.$$

Finally, the second-order cross section (9) can be cast in the following nondimensional form:

$$\tilde{\sigma}_2(\Omega) \equiv \omega_B\, \sigma_2(\omega) = \\ = 2\,L \int_{-\pi}^{\pi} d\theta \int_0^{K_L(\theta)} \tilde{I}(K_1, \theta) \frac{\sin^2[\pi L\,(\tilde{\chi} - 1)]}{[\pi L\,(\tilde{\chi} - 1)]^2}\, K_1\, dK_1 \tag{10}$$

where

$$\tilde{I}(K_1, \theta) = 2^3 \pi^2 \Omega^{-1} |\tilde{\Gamma}|^2\, \tilde{S}(\tilde{\chi}\mathbf{K}_1) \tilde{S}(\tilde{\chi}\mathbf{K}_2)\, \tilde{\chi}^5. \tag{11}$$

Making use of the symmetry of the integrand with respect to the q–axis, we integrate over the right half plane only (see Fig. 4), which is specified by the limits $\pm K_L$

$$K_L(\theta) = \begin{cases} (2|\cos\theta|)^{-1}, & -\pi < \theta < -\frac{\pi}{2} \\ \infty, & -\frac{\pi}{2} < \theta < \frac{\pi}{2} \\ (2|\cos\theta|)^{-1}, & \frac{\pi}{2} < \theta < \pi \end{cases}$$

and multiply the result by a factor of two.

B. Continuum

In this section, we focus upon the base of the second-order spectrum which we refer to as "the continuum."

Since the parameter L is assumed to be large, the squared Dirichlet function is rapidly oscillating and the integral can be evaluated employing standard asymptotic techniques, of which the simplest is the "stationary phase method" (e.g., [14]). Expanding in (10) the argument of the Dirichlet function near a stationary point K_s in the integrand, we get

$$\tilde{\chi} - 1 = \frac{\partial\tilde{\chi}}{\partial K_1}(K_1 - K_s) + \frac{1}{2}\frac{\partial^2\tilde{\chi}}{\partial K_1^2}(K_1 - K_s)^2 + O\left[(K_1 - K_s)^3\right] \tag{12}$$

where $K_s = K_s(\theta)$ is implicitly specified by the equation $\chi(\Omega, K_s, \theta) = 1$, which is equivalent to

$$\Omega = {K_s}^{1/2} + (K_s^2 + 2K_s\cos\theta + 1)^{1/4}. \tag{13}$$

When the integration domain does not contain the origin, that is, for frequencies $\Omega \neq \sqrt{2}$, the first derivative χ_{K_1} does not vanish and the saddle-point evaluation gives

$$\tilde{\sigma}_2(\Omega) = 2\int_{-\theta_L}^{\theta_L} \tilde{I}(K_s, \theta) \frac{K_s}{|\tilde{\chi}'_{K_1}|}\bigg|_{K_1 = K_s} d\theta + O\left[\frac{1}{(L|\tilde{\chi}'_{K_1}|)^2}\right]. \tag{14}$$

The limits θ_L are determined by the condition of intersection of the contour $\tilde{\chi}(\Omega, K_s, \theta) = 1$ with the axis $(0, q)$

$$\theta_L = \begin{cases} \pi, & \Omega < \sqrt{2} \\ \pi - \arccos\left(\frac{2}{\Omega^2}\right), & \Omega > \sqrt{2} \end{cases}.$$

The derivative χ'_{K_1} should be evaluated at $K_1 = K_s$, which yields

$$\tilde{\chi}'_{K_1} = -\frac{\tilde{\chi}^{3/2}}{\Omega}\left[\frac{1}{{K_s}^{1/2}} + \frac{K_s + \cos\theta}{(K_s^2 + 2K_s\cos\theta + 1)^{3/4}}\right]. \tag{15}$$

As one might expect, the main term in (14) exactly coincides with the cross-section formula by Lipa and Barrick [7]. This formula is valid for all frequencies except when Ω is sufficiently

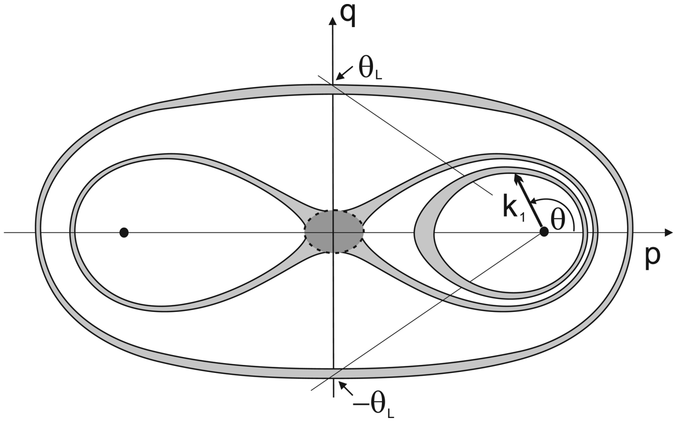

Fig. 4. Integration domains (light gray color) which contribute to the continuum.

close to $\sqrt{2}$. We outline the limitations on the use of Barrick's formula (14).

The necessary condition for validity of the asymptotic expansion (14) requires

$$(L|\tilde{\chi}'_{K_1}|)^{-2} \ll 1$$

which results in the constraint $|\tilde{\chi}'_{K_1}| \gg 1/L$. The derivative $\tilde{\chi}'_{K_1}$ tends to zero as $\theta \to \pi$ and $K_s \to 1/2$. The expansion about this point yields the results dependent on the direction from which the point is approached

$$\tilde{\chi}'_{K_1} \approx \Omega\,(\Omega^2 - 2), \qquad (\Omega > \sqrt{2})$$
$$\tilde{\chi}'_{K_1} \approx \Omega\,(2 - \Omega^2)^{1/2}, \qquad (\Omega < \sqrt{2}).$$

It is easy to see that the asymptotic expansion (14) is valid for frequencies $\Omega < \sqrt{2} - O(1/L^2)$ or $\Omega > \sqrt{2} + O(1/L)$ and has the accuracy

$$\frac{1}{L|\tilde{\chi}'_{K_1}|} = \begin{cases} \left[L\Omega(2-\Omega^2)^{1/2}\right]^{-1}, & \Omega < \sqrt{2} - L^{-2} \\ \left[L\Omega(\Omega^2-2)\right]^{-1}, & \Omega > \sqrt{2}L^{-1}. \end{cases}$$

Thus, we conclude that the asymptotic formula for the second-order continuum, which we derived for the finite-length pulses, shows that to the leading order in the pulse length L the height of the continuum does not depend on L, while the L-dependent terms are $O(1/L)$ small.

Strictly speaking, we should have carried out summation over all stationary points corresponding to local maxima of the squared Dirichlet function; however, the contribution of the second maximum is less than 5% of the first one and, therefore, in the context of analysis of the already small second-order peaks, we can neglect all stationary points except the main one.

C. Second Harmonic Peak

The "second-harmonic" peak appears at the nondimensional Doppler frequency $\Omega_h = \sqrt{2}$, where the integration domain turns from the ellipse-like figures into the "eight" (see Fig. 4). At the center of the "eight," the first derivative $\partial\tilde{\chi}/\partial K_1$ in (12) vanishes and a saddle-point appears.

To evaluate the integral by employing asymptotic expansions, first split the integration domain in (p, q) into two parts: 1) $0 < 2\tilde{p}^2 + 4\tilde{q}^2 < r_o^2$, where $r_o^2 = 2\tilde{p}_o^2 + 4\tilde{q}_o^2 \ll 1$; and 2) $r_o^2 < 2\tilde{p}^2 + 4\tilde{q}^2 < \infty$. Correspondingly, we introduce two integrals $\tilde{\sigma}_f(\Delta)$ over the region 1) and $\tilde{\sigma}_{sl}(\Omega)$ over the region 2)

$$\tilde{\sigma}_f = \int\int_0^{r_o} \ldots d\tilde{p}d\tilde{q} \quad \tilde{\sigma}_{sl} = \int\int_{r_o}^{\infty} \ldots d\tilde{p}d\tilde{q}. \qquad (16)$$

The integrals $\tilde{\sigma}_f$ and $\tilde{\sigma}_{sl}$ can be viewed, respectively, as the *inner* and *outer* expansions of the cross-section formula (10). The inner solution $\tilde{\sigma}_f$ will be obtained in the form of asymptotic expansion with respect to small parameter $Lr_o^4 \ll 1$, while the outer expansion $\tilde{\sigma}_{sl}$ will be expressed in terms of power series in $r_o \ll 1$. After matching the outer and inner expansions, the value of r_o drops out of the sum of $\tilde{\sigma}_f$ and $\tilde{\sigma}_{sl}$ and we get the analytical representation of the integral we are looking for

$$\tilde{\sigma}_2(\Omega) = \tilde{\sigma}_f(\Delta) + \tilde{\sigma}_{sl}(\Omega) + O\big[(Lr_o)^{-1}\big] \qquad (17)$$

where $\tilde{\sigma}_f(\Delta)$ is a function of only the *fast* variable

$$\Delta \equiv 2\pi L\left(\frac{\Omega}{\Omega_h} - 1\right), \qquad (\Omega_h = \sqrt{2})$$

while $\tilde{\sigma}_{sl}(\Omega)$ depends on the *slow* variable Ω. Detailed derivation of $\tilde{\sigma}_f$ and $\tilde{\sigma}_{sl}$ is given in Appendices A1 and A2, respectively). Here, we present just the final results for the fast and slow parts, respectively

$$\tilde{\sigma}_f(\Delta) = \frac{\tilde{I}_o}{2^{1/2}}\left(\ln L - \ln|\Delta| + C_2 + Ci(2\Delta) - \frac{\sin 2\Delta}{2\Delta}\right) \quad (18)$$

$$\tilde{\sigma}_{sl}(\Omega) = -\frac{\tilde{I}_o}{2^{1/2}}\left(\ln\left[\frac{11}{16}\right] + \int_0^1\left[2^{5/2}\frac{\tilde{I}(z)}{\tilde{I}_o}\frac{K_s}{|\tilde{\chi}'_{K_1}|}\frac{\partial\theta_s}{\partial z} + \frac{1}{z}\right]dz\right) \quad (19)$$

where $\tilde{I}_o$ is the value of $\tilde{I}_o$ specified by (11) taken in the center of the "eight" [see also (34)], Ci is the integral cosine, and C_2 is a fixed constant ($C_2 = 1.14473$).

Formulas (17)–(19) also enable us to estimate the frequency shift (which we denote as $\delta\Omega$ and $\delta\Delta$ for the slow and fast variables, respectively) of the maximum of the second harmonic peak from its "right" value Ω_h due to the effect of the continuum. The shift $\delta\Omega$ is determined from the condition

$$\tilde{\sigma}'_2(\Omega_h + \delta\Omega) = 2^{1/2}\pi L\,\tilde{\sigma}'_f(\Delta_h + \delta\Delta) + \tilde{\sigma}'_{sl}(\Omega_h + \delta\Omega) = 0. \quad (20)$$

Expanding the functions with respect to small $\delta\Delta$ and $\delta\Omega$, we find

$$\delta\Omega = -\frac{1}{2\pi^2 L^2\,\tilde{\sigma}''_f(\Delta_h)}\,\tilde{\sigma}'_{sl}(\Omega_h) = -\frac{3\,\tilde{\sigma}'_{sl}(\Omega_h)}{\pi^2 L^2\,\tilde{I}_o}. \qquad (21)$$

Here, we used the fact that $\tilde{\sigma}''_f(\Delta_h) = \tilde{I}_o/6$.

Thus, the shift being $O(L^{-2})$ is negligibly small for most conceivable applications.

D. Corner Reflection Peak

The corner reflection peak appears due to a specific condition of EM backscattering. Recall that the nondimensional coupling coefficient $\tilde{\Gamma}$ in the cross-section formula (10) consists of two parts: the hydrodynamic component $\tilde{\Gamma}_H$, and the EM component $\tilde{\Gamma}_{\mathrm{EM}}$; i.e., $\tilde{\Gamma} = \tilde{\Gamma}_H + \tilde{\Gamma}_{\mathrm{EM}}$. In the polar coordinates (R, ψ), the nondimensional EM coefficient $\tilde{\Gamma}_{\mathrm{EM}}$ acquires the form

$$\tilde{\Gamma}_{\mathrm{EM}} = \frac{-\frac{1}{4} - R\sin^2\psi + 2R}{\sqrt{1-4R} - \tilde{\Delta}_w}.$$

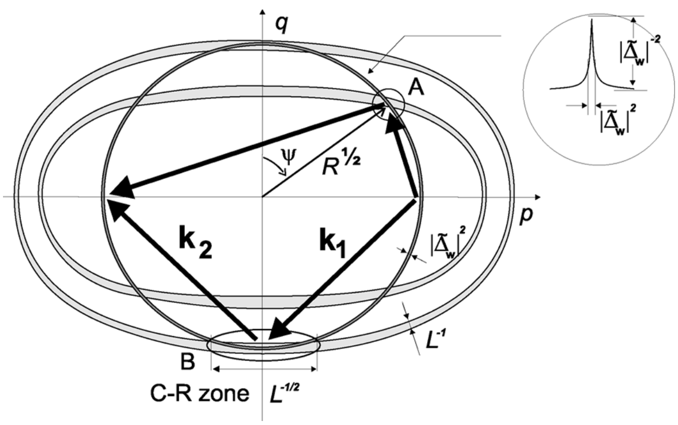

Fig. 5. Main contributions to the second-order cross section $\tilde\sigma_2$ due to the EM coefficient $\tilde\Gamma_{\rm EM}$. The circle of radius $R = (1/2)^2$ indicates the position of the maximum of $\tilde\Gamma_{\rm EM}$, while the encircled insertion in the top-right corner illustrates the fact that the amplitude of the maximum and its width are $|\tilde\Delta_w|^2$ and $|\tilde\Delta_w|^{-2}$, respectively. The width of the constant frequency contours and the width of the corner reflection peak zone are shown to be scaled as L^{-1} and $L^{-1/2}$.

The Cartesian coordinates $(\tilde p, \tilde q)$ are expressed in terms of (R, ψ) as

$$\tilde p = R^{1/2}\sin\psi \quad \tilde q = R^{1/2}\cos\psi.$$

Since the impedance $\tilde\Delta_w$ is a $O(10^{-2})$ small nondimensional constant (we use for our estimates $\tilde\Delta_w = 0.011 - i\,0.012$ given in [7]), it scales the width $\sim |\tilde\Delta_w|^2 \ll 1$ and height $\sim |\tilde\Delta_w|^{-2} \gg 1$ of a sharp peak of $|\tilde\Gamma_H + \tilde\Gamma_{\rm EM}|^2$ situated on the circle of radius $R^{1/2} = 1/2$ (see Fig. 5 and its upper right insert).

This peak strongly affects the cross section near the frequency $\Omega_{\rm cr} = 2^{3/4}$. The mechanism is illustrated in Fig. 5. The second-order cross section is produced by integration along the strip of width L^{-1}. The strip can 1) intersect the circle (region "A" in Fig. 5), when the Doppler frequency is less then $2^{3/4}$, 2) be tangent to the circle (region "B"), when the Doppler frequency is close to $2^{3/4}$, and 3) not intersect the circle, when the Doppler frequency is greater then $2^{3/4}$ (not shown). One can roughly estimate the corresponding contributions to the echo from the following simple geometrical considerations.

The contribution due to region "A" equals the area of the intersection of the contour and the circle $L^{-1}|\Delta|^2$ times the value of the function at the intersection $L|\Delta|^{-2}$, which yields an $O(1)$ value. Since the contour corresponding to frequency equal to $2^{3/4}$ is tangent to the circle, the area of region "B" equals $L^{-1/2}|\Delta|^2$, while the function height remains the same, $L|\Delta|^{-2}$; this results in a $\sim L^{1/2}$ contribution. The contours with $\eta > 2^{3/4}$ and the rest of the contours with $\eta \le 2^{3/4}$ produce $O(1)$ contributions to echo.

By means of asymptotic expansions given in detail in Appendix B, the description of the second-order cross section $\tilde\sigma_2(\Omega)$ provided by (10) can be reduced to a simple closed form valid near $\Omega_{\rm cr} = 2^{3/4}$

$$\tilde\sigma_2(\Omega) = \hat I_{\rm cr}\left|\frac{4L\tilde\Delta_w^4}{3\pi}\right|^{1/2}\{\,d_0\,Sj(\zeta) + Fj(\zeta)\} + O\left[\beta, \frac{1}{L}\right]. \tag{22}$$

Here, the independent variable ζ is expressed through Ω as

$$\zeta \equiv \pi L\frac{\Omega^4 - 8}{2\Omega^4} \tag{23}$$

$\hat I_{\rm cr} \equiv \tilde I(2^{-1/2}, 3\pi/4)$ is given by (11)

$$d_0 = -2\ln\beta - 2\ln 2 - \gamma + \frac{\pi}{2}$$

($\gamma \simeq 0.577$ is the Euler constant), the small parameter β is a combination of $\tilde\Delta_w$, and $L^{1/2}$

$$\beta = {\rm Re}(\tilde\Delta_w)\left[\frac{\pi L}{4}\right]^{1/2} \ll 1. \tag{24}$$

Functions $Sj(\zeta)$ and $Fj(\zeta)$ are defined as follows:

$$\begin{aligned} Sj(\zeta) = {} & \pi\zeta^{-3/2}\left(\frac{1}{4} + \zeta\right)F_{\rm C}\left[\left(\frac{4\zeta}{\pi}\right)^{1/2}\right] - \frac{\pi^{1/2}}{2\zeta}\cos(2\zeta) \\ & + \pi\zeta^{-3/2}\left(\frac{1}{4} - \zeta\right)F_S\left[\left(\frac{4\zeta}{\pi}\right)^{1/2}\right] - \frac{\pi^{1/2}}{2\zeta}\sin(2\zeta) \end{aligned} \tag{25}$$

where F_C and F_S are the Fresnel cosine and sine integrals, and (26), shown at the bottom of the page, holds. Here, ${}_2F_3$ are the generalized hypergeometric functions given in Appendix C.

The explicit formula (22) enables us to calculate the true position of the corner reflection peak. The "ideal" unperturbed peak position is $\Omega_{\rm cr} = 2^{3/4}$ (or $\zeta = 0$ in fast variables), but, in fact, even in the absence of currents and interference with the continuum, the position of the maximum of $\tilde\sigma_2(\Omega)$ is slightly shifted. Since for the chosen representative estimate of $\tilde\Delta_w$ ($\tilde\Delta_w = 0.011 - i0.012$) and L in the range from 25 to 400, the position of the maximum varies in the range from -1.01 to -0.97, in terms of ζ, the shift is very close to -1. Using (23), one can estimate the true position of the corner reflection peak as

$$\Omega_{cr\ \rm true} = 2^{3/4} - \frac{1}{2^{1/4}\pi L}. \tag{27}$$

$$Fj(\zeta) = \pi^{1/2}\left\{4\,{}_2F_3\left[\begin{matrix}\frac{1}{4}, \frac{1}{4} \\ \frac{1}{2}, \frac{5}{4}, \frac{5}{4}\end{matrix}; -\zeta^2\right] - \frac{4}{9}\,{}_2F_3\left[\begin{matrix}\frac{3}{4}, \frac{3}{4} \\ \frac{1}{2}, \frac{7}{4}, \frac{7}{4}\end{matrix}; -\zeta^2\right]\right\} + \pi^{1/2}\zeta\left\{\frac{8}{25}\,{}_2F_3\left[\begin{matrix}\frac{5}{4}, \frac{5}{4} \\ \frac{3}{2}, \frac{9}{4}, \frac{9}{4}\end{matrix}; -\zeta^2\right] - \frac{8}{9}\,{}_2F_3\left[\begin{matrix}\frac{3}{4}, \frac{3}{4} \\ \frac{3}{2}, \frac{7}{4}, \frac{7}{4}\end{matrix}; -\zeta^2\right]\right\} \tag{26}$$

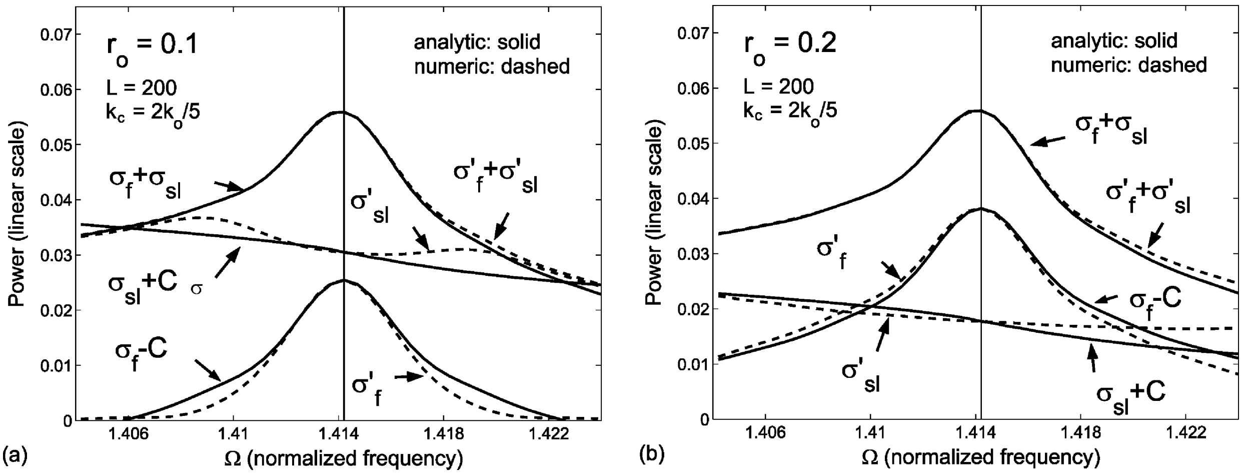

Fig. 6. Second harmonic peak: comparison between the analytical results given by $\tilde{\sigma}_f$ from (18) and $\tilde{\sigma}_{sl}$ from (19), and numerical calculation of $\tilde{\sigma}'_f$ and $\tilde{\sigma}'_{sl}$ from (16), calculations ($L = 200$, $k_c = 2k_o/5$, C is a normalization constant). (a) $r_o = 0.1$ and $C = 0.0495$. (b) $r_o = 0.2$ and $C = 0.0368$.

With the increase of our large parameter L, the corner reflection peak gets closer to its "ideal" position $2^{3/4}$, but the shift has to be taken into account for moderate lengths of the pulse.

E. Numerical Verification of Analytical Results

In this section, we carry out a verification of the analytical formulas for the second harmonic peaks (17) and the corner reflection peaks (22) by numerical calculations of the cross-section integral (10). We choose for our numerical test the following model of the ocean wave spectrum

$$S(\mathbf{k}) = S_{PM}(k)\,\Phi(\theta + \theta_{\text{wind}}) \tag{28}$$

where

$$S_{PM}(k) = 0.005\,\frac{e^{-0.74\,k_c^2/k^2}}{k^4}$$

is the Pierson–Moskowitz nondirectional spectrum with the falloff of saturated waves being specified by a falloff wave number k_c. The directional factor Φ was taken to be

$$\Phi(\theta + \theta_{\text{wind}}) = \frac{4}{3\pi}\cos^4\left[\frac{\theta + \theta_{\text{wind}}}{2}\right], \qquad (\theta_{\text{wind}} = \pi).$$

The key role of the vicinity of the origin in the formation of the second harmonic peak is illustrated in Fig. 6(a) and (b), where the results of analytical calculations of the fast-varying cross section $\tilde{\sigma}_f$ via (18), and the slow-varying cross section $\tilde{\sigma}_{sl}$ via (19), are depicted. The part $\tilde{\sigma}_f$ describes the peak itself, while $\tilde{\sigma}_{sl}$ describes its slow-varying base. The analytical results are compared with numerical calculations of the constituent integrals $\tilde{\sigma}_f$ and $\tilde{\sigma}_{sl}$ based upon (16) and (10), inside and outside of r_o, respectively. A very good agreement between analytical and numerical results is apparent, especially in Fig. 6(b). According to the results of previous sections the characteristic size of the vicinity of the origin producing the second harmonic peak is $r_o \sim L^{-1/2}$. An example with $L = 200$ ($L^{-1/2} = 0.07$) was tested with $r_o = 1.5L^{-1/2} \approx 0.1$ [Fig. 6(a)] and $r_o = 3L^{-1/2} \approx 0.2$ [Fig. 6(b)]. The choice $r_o = 1.5L^{-1/2}$ confined a too small vicinity of the origin and $\tilde{\sigma}_{sl}$ exhibited small-scale deviations from the anticipated slow-varying behavior, while the choice $r_o = 3L^{-1/2}$ provided a much cleaner split of the integral (16) into the fast- and slow-varying parts. We choose the characteristic scale of the area in the origin responsible for the peak by specifying the condition $r_o = 3L^{-1/2}$. In physical variables using the relation $r_o^2 = 2\tilde{p}_o^2 + 4\tilde{q}_o^2$, one gets $p_o = 2L^{-1/2}$ in the radar beam direction and $q_o = L^{-1/2}$ in the cross-beam direction.

The dependence of the second harmonic peak height on the normalized radar pulse length L is presented in Fig. 7(a). The parameter L is varying from 50 to 800. The greater the L, the higher and more discernible the peak becomes. We note that the power scale in Figs. 6–8 is linear, not logarithmic in decibels as is more common, since in the logarithmic scale the peaks are often poorly pronounced. The analytical results given by (17)–(19) are plotted in solid curves, while the numerical calculations based upon (10) are presented in dashed curves. Thus, both Fig. 7, and upper curves of Fig. 6 demonstrate a nearly perfect coincidence of the closed-form solution (17)–(19) with the corresponding numerical results.

The dependence of the second harmonic peak height on the falloff wave number k_c is shown in Fig. 7(b). We consider the values $k_c = 2k_o/10, 2k_o/5$, and $2k_o/3$, which, for example, for measurements by a 50-MHz radar corresponds to 30-, 15-, and 9-m wavelength of the dominant waves in the wind wave spectrum. As the length of the falloff waves increases (smaller k_c) the base (continuum) also increases making the peak itself less discernible, because the ratio of the peak height to the height of the continuum decreases. The height-dependence of the corner reflection peak on the normalized radar pulse length L is presented in Fig. 8(a). The parameter L is varying from 50 to 400. The greater L is, the higher and more discernible is the peak. Analytical results are shown in solid curves (22)–(26) while the numerical integration of (10) is plotted in dashed lines. As it is easy to see, there is a very good agreement between the analytical and numerical results. The discrepancy does not exceed 5% and is due to neglecting the terms of $O(\beta)$ in (22). The figure also confirms that, in full accordance with (27), as L grows, the peak maximum approaches its "ideal" position $\Omega_{\text{cr}} = 2^{3/4}$. It

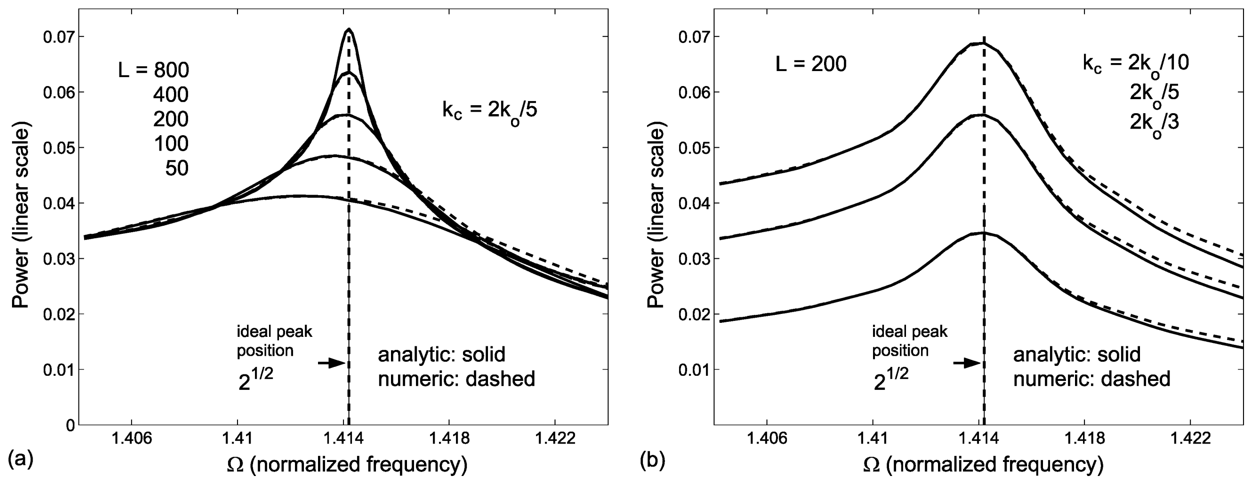

Fig. 7. Second harmonic peak: comparison between the analytical results given by (17)–(19) and numerical calculations based on (16). (a) $k_c = 2k_o/5$ and $L =$ (50, 100, 200, 400, 800). (b) $L = 200$ and $k_c = (2k_o/10,\ 2k_o/5,\ 2k_o/3)$.

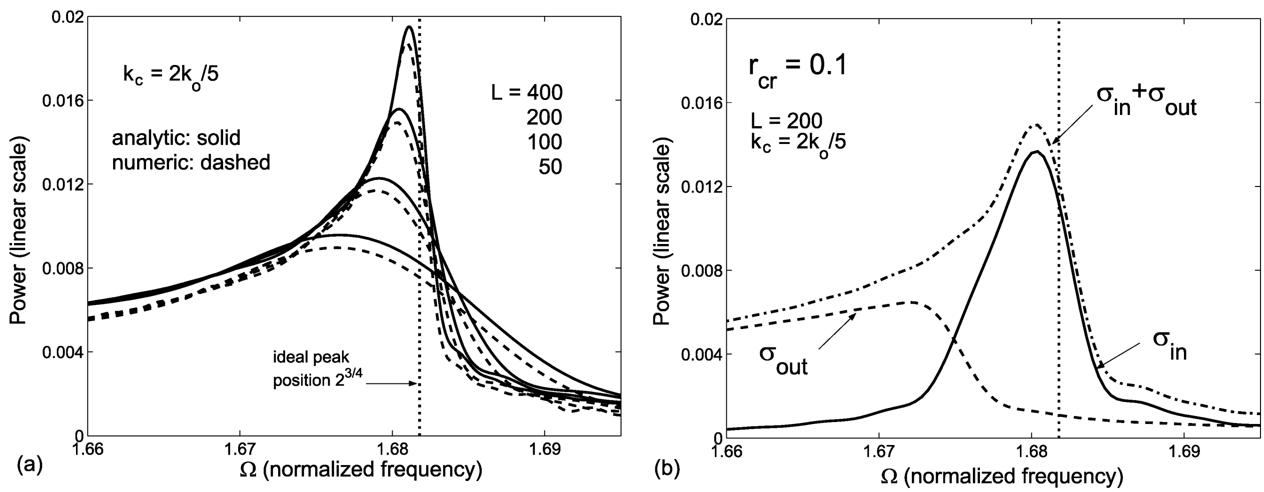

Fig. 8. Corner reflection peak. (a) Comparison of analytical results given by (22) and numerical calculations based upon (10), $k_c = 2k_o/5$, $L =$ (50, 100, 200, 400). (b) Role of the vicinity of the corner reflection region in forming the peak, $\tilde{\sigma}_{\rm in}$ is calculated from (10) for $p^2 + 2(q - 1/2)^2 < r_{\rm cr}^2$, and $\tilde{\sigma}_{\rm out}$ is for $p^2 + 2(q - 1/2)^2 > r_{\rm cr}^2$ ($L = 200$ and $r_{\rm cr} = 0.1$).

is also worth noting that (22), on the one hand, catches the peak "fast"-frequency behavior (23) and, on the other hand, matches perfectly with the "slow"-frequency region far away from the peak.

For the corner reflection peaks, the role of the vicinity of the corner reflection region in forming the peak is illustrated in Fig. 8(b). The results of numerical calculations of (10) inside and outside the corner reflection region $p^2 + 2(q-1/2)^2 < r_{\rm cr}^2$ are shown; the appropriate curves are marked as $\tilde{\sigma}_{\rm in}$ and $\tilde{\sigma}_{\rm out}$. It is again demonstrated that integration over the corner reflection region produces the peak itself, while the rest of the plane provides the continuum. The rough estimate of the linear sizes of the corner reflection region forming the peak $L^{-1/2} \times L^{-1/2}$ proves to be quite good and can be recommended for use for a wide range of parameters.

IV. Concluding Remarks

We revisited the classical problem of EM scattering by the sea surface in the Bragg regime from the second-order Doppler spectra perspective. The Doppler spectra of the second-order cross section has been long known to consist of the three different parts: continuum and two distinct pairs of peaks, namely, the *second harmonics* and *corner reflection* pairs of peaks. This paper is the first one focussed primarily upon the properties of these peaks, qualitative and quantitative. First, we briefly summarize the main results. The key finding is in revealing the singular nature of these peaks: The main (singular) contribution is shown to be due to particular pairs of waves and their immediate neighbors, although waves of many different wavelengths and directions do contribute to these peaks. This fact opens the principal possibility to employ these peaks in remote sensing of vertical profiles of surface currents, which was the prime motivation of this paper.

However, at the next level, we encounter another group of major questions, which have to be clarified before conceiving any practical applications. The questions are concerned with the manifestations of these peaks in a more realistic problem setting, which necessarily includes the EM pulses of finite length and beam width. The basic question is how sensitive are the positions of these peaks with respect to external parameters of the

EM pulses. Only if the positions are robust, then the questions on the dependence of the peak parameters on all sorts of factors become also of importance.

We confined our analysis to clarifying the previous questions for the EM pulses of finite duration, neglecting the effects of finite aperture. We expect the finite aperture effects to be qualitatively similar to those due to the finite duration. Simultaneous analysis of two factors, although certainly doable, would have been too involved. Under these assumptions employing an asymptotic expansions based upon smallness of $1/L$, we found the Doppler spectra of the second-order cross section, including the shape and parameters of the peaks explicitly expressed in terms of L and the normalized water impedance $\tilde{\Delta}_w$.

The second-order continuum, the smooth part of the spectrum, is due to ocean waves of various lengths and directions. As expected, the height of the continuum is not sensitive to L and is of the order of unity $\sigma_2 \sim 1$.

The second harmonic peak arises due to the first-order Bragg scatter from the second harmonics of those components of ocean wave nonlinear field which are close to the Bragg wave: $|\mathbf{k} - \mathbf{k_B}| < L^{-1/2}k_B$. Hence, for long radar impulses with $L \gg 1$, the peak is linked to the particular scatter from the second harmonic. The second-order continuum inevitably shifts the peak position; and the answer to the principal question—whether this shift should be taken into account, proved to be negative: The shift is $\sim \Omega_B/L^2$ and can be neglected in most situations. The height of the second harmonic peak (due to the smeared "singularity") weakly depends on the pulse length

$$\sigma_{\sqrt{2}} \sim \ln L$$

while its width is $\sim \Omega_B/L$. The examples in Fig. 7 show that the height should be measured from the base given by the continuum, but not from the base of the spectrum, which has practical implications for the commonly used "centroid technique" for finding the position of peaks. (In this technique one determines the peak center by the -3-dB criterion.)

The corner reflection peak arises due to the second-order EM scatter from two components of first-order ocean wave field, which we denote as $\mathbf{k_{3/4}}$, with the wavelengths $\sqrt{2}k_B$ and directions $\pm\pi/4$ to the radar beam. The immediate vicinity of these components contributing to the peak is specified by the inequality $|\mathbf{k} - \mathbf{k_{3/4}}| < L^{-1/2}k_B$. The position of the peak is always shifted towards the lower frequencies, with the magnitude of the shift given by an expression of ultimate simplicity: $\Omega_B/(2^{1/4}\pi L)$. Although the shift is relatively small, it has to be taken into account in processing the data for measuring currents in case of not too long pulses.

The height of the corner reflection peak slowly increases with the length of the pulse

$$\sigma_{\rm cr} \sim L^{1/2}\tilde{\Delta}_w^2$$

while its width is inversely proportional to the pulse length $\sim \Omega_B/L$. Strong dependence of the peak height on the salinity sensitive sea surface impedance Δ_w, which might be potentially used for spotting lenses of fresh water or marking the boundaries of river plumes, is also worth noting.

The derived explicit asymptotic formulas for the second-order spectra have been verified numerically. Nearly perfect agreement was found for a wide range of tested examples. Hence, once again, we have confirmed that the second-order peaks arise due to singular contributions of particular spectral components of the ocean wave field and that the derived analytic formulas can be recommended for practical use. Certainly, in most of practical HF radar applications, both the finite length of the pulse and the finite aperture of the radar should be taken into account. However, very often one of those factors is dominant; then, we either come back to the situation we just analyzed, or, to the very similar situation which is qualitatively the same and can be treated in a similar fashion.

Since the peak positions are firmly linked with the frequencies of these components and the shifts due to the continuum are either negligible (the second harmonic peak) or could be easily taken into account using very simple formulas (the corner reflection peak), this justifies the use of these peaks for measuring the currents in the same manner as the main Bragg lines in the Doppler spectrum, with the correction $\sim -\omega_B/L$ for the corner reflection peak position taken into account.

The derived formulas enable us to quantify some of the possible systematic errors of measurements by means of the second-order peaks. A small-scale field experiment aimed at testing the possibility of measuring the surface current vertical profile by utilizing the second-order peaks was successful [11], [12], although now, by taking into account the correction to the position of the corner reflection peaks, we could have further increased the accuracy of the radar measurements. We can now conclude that the theoretical foundation for a method of probing the surface current shear by ground-based single-frequency HF radars has been firmly established.

Our paper also paved the way for addressing the key practical question on when the second-order peaks are visible and can be used for current measurements. The results imply that the ways of distinguishing the second-order peaks should be changed. In particular, the derived expressions for the peaks enable one to employ more sophisticated data processing algorithms; now, we know where and how to look for these peaks. Then, the second-order peaks could be made visible in a wider class of situations and at worse SNR than is common at present.

Furthermore, it is worth noting that the current analysis can be extended to EM scattering from the sea surface for bistatic radars. Although the "bistatic" second-order peaks appear at different positions in the "bistatic" spectrum, their physics is the same as in the monostatic case.

Appendix A
Second Harmonic Peak

1) Splitting of the Integration Domain: In this appendix, we provide the somewhat cumbersome details of derivation of the closed-form analytical description of the "second harmonic" peak given by (17)–(19). The peak appears at the nondimensional Doppler frequency $\Omega_h = 2^{1/2}$, when the integration domain turns from the ellipse-like figures into the "eight" shown in Fig. 4. At the center of the "eight," the first derivative $\partial\tilde{\chi}/\partial K_1$ in (12) becomes zero and a saddle-point appears.

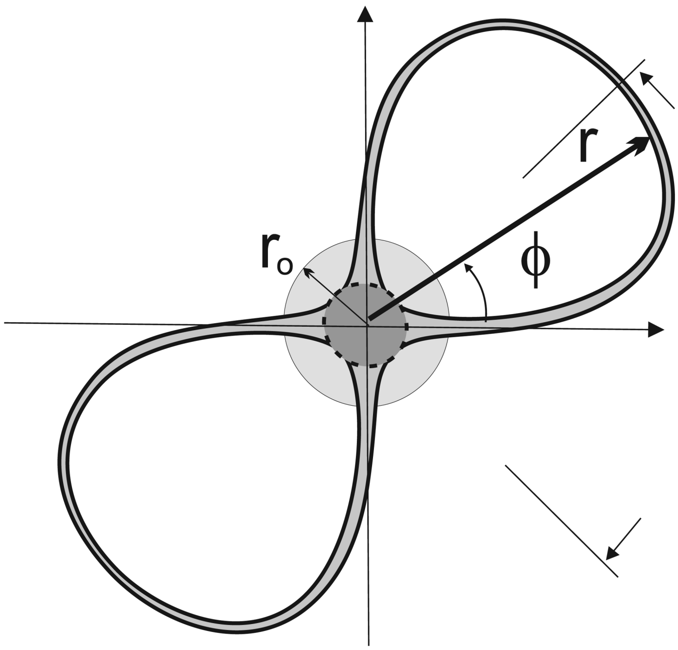

Fig. 9. Integration domain in the polar coordinates (r, ϕ) at $\Omega_h = 2^{1/2}$.

To clarify the situation near the saddle point it is convenient to rewrite the integral in polar coordinates (r, ϕ) related with the nondimensional Cartesian coordinates $(\tilde{p}, \tilde{q})$ in a nonstandard way

$$\tilde{p} = \frac{r}{2}(\cos\phi + \sin\phi) \quad \tilde{q} = \frac{r}{2^{3/2}}(-\cos\phi + \sin\phi). \tag{29}$$

This particular choice of new variables is prompted by a very simple form that $\tilde{\chi}(\Omega_h)$ takes in these new coordinates

$$\tilde{\chi}(\Omega_h) = 1 + \sum_{n=1}^{\infty} P_n(\sin 2\phi)\, r^{2n}$$

where P_n is a polynomial of the nth order.

Then, the integration domain at $\Omega_h = 2^{1/2}$ takes the form shown in Fig. 9 and the modified Barrick's formula (10) for the second-order cross section reads

$$\tilde{\sigma}_2(\Omega) = \frac{4}{2^{3/2}} L \int_0^{\infty} \int_{-\pi/4}^{\pi/4} \tilde{I}(r,\phi)\, S\left[\pi L(\tilde{\chi} - 1)\right] r dr d\phi \tag{30}$$

where $\tilde{I}(r,\phi) \equiv \tilde{I}(K_1, \theta)$. The central symmetry property was used, so that the integral is taken over one fourth of the plane for ϕ from $-\pi/4$ to $\pi/4$ (see Fig. 9) and multiplied by four.

To evaluate the integral by employing asymptotic expansions, first split the integration domain in r into two parts as follows: 1) from zero to $r_o \ll 1$ and 2) from r_o to ∞. Correspondingly, we introduce two integrals σ_f and σ_{sl}

$$\tilde{\sigma}_2 = \tilde{\sigma}_f + \tilde{\sigma}_{sl}, \; \tilde{\sigma}_f = \int_0^{r_o} \{\ldots\} dr \quad \tilde{\sigma}_{sl} = \int_{r_o}^{\infty} \{\ldots\} dr. \tag{31}$$

The integrals $\tilde{\sigma}_f$ and $\tilde{\sigma}_{sl}$ can be viewed, respectively, as the *inner* and *outer* expansions. The inner solution $\tilde{\sigma}_f$ can be obtained in the form of asymptotic expansion with respect to small parameter $Lr_o^4 \ll 1$, while the outer solution $\tilde{\sigma}_{sl}$ can be expanded into power series in $r_o \ll 1$. After matching the outer and inner solutions, the value of r_o drops out of the final result $\tilde{\sigma}_2 = \tilde{\sigma}_f + \tilde{\sigma}_{sl}$ and we get the analytical representation of the integral we sought.

2) Integration Near the Origin: Let us consider the inner expansion for $\tilde{\sigma}_f$ in detail. Starting with (30) and simplifying it by the substitution $z = \sin 2\phi$, we find

$$\tilde{\sigma}_f(\Omega) = \frac{L}{2^{1/2}} \int_0^{r_o} \int_{-1}^{1} \tilde{I}(r,z)\, s\left[\pi L(\tilde{\chi} - 1)\right] r dr \frac{dz}{\sqrt{1 - z^2}}. \tag{32}$$

Expanding the argument of the "fast" function in powers of r^2, z, and Ω, we find

$$\begin{aligned}\tilde{\chi} - 1 &= 2\left(\frac{\Omega}{\Omega_h} - 1\right) + \frac{1}{2} r^2 z + O\left[r^4, \left(\frac{\Omega}{\Omega_h} - 1\right)^2\right] = \\ &= \frac{\rho z}{\pi L} + \frac{\Delta}{\pi L} + O\left[\frac{\rho^2}{L^2}, \frac{\Delta^2}{L^2}\right]\end{aligned} \tag{33}$$

where the newly introduced variables are $\rho = \pi L r^2/2$ and $\Delta = 2\pi L(\Omega/\Omega_h - 1)$; the latter is the frequency mismatch from $\Omega_h = 2^{1/2}$.

Changing r to ρ in (32) and expanding the integrand near the origin with respect to small parameters $\rho/L \ll 1$ and $\Delta^2/L \ll 1$, we simplify the kernel as follows. Using (29), one has for $\tilde{I}(p, q)$

$$\begin{aligned}\tilde{I}(r,z) &\equiv \tilde{I}(p,q) \approx \tilde{I}_o + \tilde{I}_{\tilde{p}}\tilde{p} + \tilde{I}_{\tilde{q}}\tilde{q} + O\left[\tilde{p}^2, \tilde{q}^2, \tilde{p}\tilde{q}\right] \\ &= \tilde{I}_o + O\left[\frac{\rho}{L}\right], \qquad (\tilde{I}_o \equiv \tilde{I}(0,0))\end{aligned} \tag{34}$$

since $\tilde{I}_{\tilde{p}} = \tilde{I}_{\tilde{q}} = 0$ at $(\tilde{p}, \tilde{q}) = 0$ because of the central symmetry. Then

$$\tilde{I}(r,z)\, s\left[\pi L(\tilde{\chi} - 1)\right] \approx \tilde{I}_o \frac{\sin^2(\rho z + \Delta)}{(\rho z + \Delta)^2} + O\left[\frac{\rho}{L}, \frac{\Delta^2}{L}\right]. \tag{35}$$

Thus, we find

$$\tilde{\sigma}_f(\Delta) = \frac{\tilde{I}_o}{2^{1/2}\pi} \int_0^{\rho_o} \int_{-1}^{1} \frac{\sin^2(\rho z + \Delta)}{(\rho z + \Delta)^2} \frac{d\rho\, dz}{\sqrt{1 - z^2}} + O\left[\frac{\rho_o^2}{L}, \frac{\rho_o \Delta^2}{L}\right] \tag{36}$$

where $\rho_o = \pi L r_o^2/2$.

Integral (36) can be represented as a power series in Δ

$$\tilde{\sigma}_f(\Delta) = \frac{\tilde{I}_o}{2^{1/2}} \sum_{n=0}^{\infty} \frac{\Delta^n}{n!} \tilde{\sigma}_f^{(n)}(\rho_o) + O\left[\frac{\rho_o^2}{L}, \frac{\rho_o \Delta^2}{L}\right]$$

where

$$\tilde{\sigma}_f^{(n)}(\rho_o) = \frac{1}{\pi} \int_{-1}^{1} \frac{dz}{\sqrt{1 - z^2}} \int_0^{\rho_o} \frac{d^n}{d\Delta^n} \left[\frac{\sin^2(\rho z + \Delta)}{(\rho z + \Delta)^2}\right]\Bigg|_{\Delta = 0} d\rho. \tag{37}$$

For $n = 0$, the integral can be explicitly expressed in terms of a generalized hypergeometric function ${}_2F_3$ (see Appendix C)

$$\tilde{\sigma}_f^{(0)}(\rho_o) = \rho_o\, {}_2F_3\left[\frac{1}{2},\frac{1}{2};\frac{3}{2},\frac{3}{2},2;-\rho_o^2\right] \tag{38}$$

which, for large values of ρ_o, has the following asymptotics (see also Appendix C):

$${}_2F_3\left[\frac{1}{2},\frac{1}{2};\frac{3}{2},\frac{3}{2},2;-\rho_o^2\right] = \frac{\ln\rho_o + C_1}{\rho_o} + O\left[\frac{1}{\rho_o^3}\right]$$

where $C_1 \approx 0.96351$. Then

$$\tilde{\sigma}_f^{(0)}(\rho_o) = \ln\rho_o + C_1 + O\left[\frac{1}{\rho_o^2}\right]. \tag{39}$$

For $n \geq 1$, the values of $\sigma_f^{(n)}$ can be found as follows. Using the fact that

$$\frac{d^n}{d\Delta^n}\left[\frac{\sin^2(\rho z+\Delta)}{(\rho z+\Delta)^2}\right]\Bigg|_{\Delta=0} = \frac{1}{z^n}\frac{d^n}{d\rho^n}\left[\frac{\sin^2(\rho z)}{(\rho z)^2}\right] \tag{40}$$

we get

$$\int_0^{\rho_o}\frac{d^n}{d\Delta^n}\left[\frac{\sin^2(\rho z+\Delta)}{(\rho z+\Delta)^2}\right]\Bigg|_{\Delta=0} d\rho = \frac{1}{z^n}\,\frac{d^{n-1}}{d\rho^{n-1}}\left[\frac{\sin^2(\rho z)}{(\rho z)^2}\right]\Bigg|_{\rho=0}^{\rho=\rho_o}.$$

Then, the integral (37) becomes

$$\tilde{\sigma}_f^{(2n)}(\rho_o) = \frac{1}{\pi}\left[\frac{d^{2n-1}}{d\rho^{2n-1}}\int_{-1}^{1}\frac{\sin^2(\rho z)\,dz}{(\rho z)^2 z^{2n}\sqrt{1-z^2}}\right]\Bigg|_{\rho=0}^{\rho=\rho_o} \tag{41}$$

where only even indices $2n$ are kept since for odd indices, $\tilde{\sigma}_f^{(2n+1)} \equiv 0$. Hence, $\tilde{\sigma}_f(\Delta)$ is an even function of Δ. The integrals (41) can be expressed via the hypergeometric functions ${}_1F_2$

$$\tilde{\sigma}_f^{(2n)}(\rho_o) = \frac{(-1)^n\, 2^{2n+1}}{(2n+2)!}\left[\frac{d^{2n-1}}{d\rho^{2n-1}}f(\rho;n)\right]\Bigg|_{\rho=0}^{\rho_o}$$

where

$$f(\rho;n) = \rho^{2n}{}_1F_2\left[\frac{1}{2};\frac{3}{2}+n,2+n;-\rho^2\right].$$

Employing the large ρ asymptotics of this hypergeometric function (see [15])

$${}_1F_2\left[\frac{1}{2};\frac{3}{2}+n,2+n;-\rho^2\right] = \frac{(n+1)}{\rho} + O[\rho^{-3}] \tag{42}$$

it is straightforward to find that

$$\tilde{\sigma}_f^{(2n)}(\rho_o) = \frac{(-1)^n\, 2^{2n+1}\,(n+1)}{(2n+2)(2n+1)(2n)} + O[\rho_o^{-2}]$$

or, finally, using (39)

$$\begin{aligned}\tilde{\sigma}_f(\Delta) &= \frac{I_o}{2^{1/2}}\left[\ln\rho_o + C_1 + \sum_{n=1}^{\infty}\frac{(-4)^n(n+1)}{n(2n+2)!}\Delta^{2n}\right] \\ &\quad + O\left[\frac{1}{\rho_o^2},\frac{\rho_o^2}{L},\frac{\rho_o\Delta^2}{L}\right] \\ &= \frac{\tilde{I}_0}{2^{1/2}}\left[\ln L + 2\ln r_o + C_2 + Ci(2\Delta) - \ln|\Delta| - \frac{\sin 2\Delta}{2\Delta}\right] \\ &\quad + O\left[\frac{1}{\rho_o^2},\frac{\rho_o^2}{L},\frac{\rho_o\Delta^2}{L}\right]\end{aligned} \tag{43}$$

where $Ci(\ldots)$ is the integral cosine function and C_2 is a known constant ($C_2 = C_1 + 1 - \gamma + \ln\pi - 2\ln 2 \approx 1.14473$), while $\gamma \approx 0.5772$ is the Euler's constant [15].

3) Integration From r_o to ∞ : In this section, we consider the outer solution $\tilde{\sigma}_{sl}$ near the second harmonic peak $\Omega_h = 2^{1/2}$. The contribution to the cross section due to the integration along the loop is given by the integral (14) [here, we slightly rewrite integral (14), using the symmetry of K_s and $|\chi'_{K_1}|$ with respect to θ]

$$\tilde{\sigma}_{sl}(\Omega) = 2\int_{-\theta_o}^{0}[\tilde{I}(K_s,\theta) + \tilde{I}(K_s,-\theta)]\,\frac{K_s}{|\chi'_{K_1}|}\Bigg|_{K_1=K_s} d\theta \tag{44}$$

where $K_s = K_s(\theta)$ is specified implicitly by the condition $\chi(K_s,\theta,\Omega) - 1 = 0$. The integration region from $-\theta_o$ to zero was chosen in such a way that it corresponds to the integration over ϕ in (30). The value $-\theta_o$ specifies the boundary of the saddle-point region (see Fig. 4) where integrals (32) and (44) should match.

The final aim of this section is to get the outer solution in the form of an expansion in r_o to match this outer expansion at $r_o \ll 1$ with an inner expansion at $Lr_o^2 \gg 1$.

The integral in question (44) diverges when $\theta_o \to \pi$ and $\Omega \to \Omega_h$. Let us find first the precise type of the singularity. To this end, we again change the variables $\theta = -\pi + \delta\theta$ and $\Omega = \Omega_h(1+d)$ and solve the saddle-point condition (13)

$${K_s}^{1/2} + (K_s^2 - 2K_s\cos\delta\theta + 1)^{1/4} = \Omega_h(1+d) \tag{45}$$

at small $\delta\theta \ll 1$ and $d \ll 1$. The scaling $\delta\theta = \epsilon\delta\Theta$ and $d = \epsilon^3 D$ with $\epsilon \ll 1$ yields an expansion in powers of ϵ

$$K_s = \frac{1}{2} - \frac{\epsilon}{2^{1/2}}\,\delta\Theta + O(\epsilon^2). \tag{46}$$

Similarly, other components of the integrand can be also represented as expansions in powers in ϵ

$$\tilde{\chi}'_{K_1} = -\,2^{1/2}\epsilon\,\delta\Theta + O(\epsilon^2) \tag{47}$$

$$\tilde{I} = \tilde{I}_o + O(\epsilon) \tag{48}$$

where $\tilde{I}_o$ is the same as in (36).

Hence, on combining the power expansions (46)–(48) together, it is easy to see that the integrand behaves as

$$\frac{2\,[\tilde{I}_+ + \tilde{I}_-]\,K_s}{|\tilde{\chi}'_{K_1}|} = \frac{1}{\epsilon}\frac{2^{1/2}\tilde{I}_o}{\delta\Theta} + O(1) = \frac{2^{1/2}\tilde{I}_o}{\delta\theta} + O(1)$$

where $\tilde{I}_+ = \tilde{I}(K_s, -\pi + \delta\theta)$ and $\tilde{I}_- = \tilde{I}(K_s, \pi - \delta\theta)$.

Then, the integral in (44) can be represented as a sum of the singular and regular parts as follows:

$$\begin{aligned}\tilde{\sigma}_{sl}(\Omega) &= 2^{1/2}\tilde{I}_o\int_{\delta\theta_o}^{\pi}\frac{d[\delta\theta]}{\delta\theta} + \int_{\delta\theta_o}^{\pi}\left[\frac{2[\tilde{I}_+ + \tilde{I}_-]K_s}{|\tilde{\chi}'_{K_1}|} - \frac{2^{1/2}\tilde{I}_o}{\delta\theta}\right]d[\delta\theta]\\ &= 2^{1/2}\tilde{I}_o\ln\left[\frac{\pi}{\delta\theta_o}\right]\\ &\quad + \int_0^{\pi}\left[\frac{2[\tilde{I}_+ + \tilde{I}_-]K_s}{|\tilde{\chi}'_{K_1}|} - \frac{2^{1/2}\tilde{I}_o}{\delta\theta}\right]d[\delta\theta] + O(\delta\theta_o) \qquad (49)\end{aligned}$$

where $\delta\theta_o = \pi - \theta_o$.

To match $\tilde{\sigma}_{sl}$ with the inner expansion $\tilde{\sigma}_f$, we express $\delta\theta_o$ through r_o using the definition of the new variables (29)

$$\tilde{p} = \frac{r}{2}(\cos\phi + \sin\phi) \quad \tilde{q} = \frac{r}{2^{3/2}}(-\cos\phi + \sin\phi)$$

together with

$$\tilde{p} = K_s\sin(\pi - \delta\theta) \quad \tilde{q} = \frac{1}{2} + K_s\cos(\pi - \delta\theta)$$

and (46). Then

$$\delta\theta_o = \frac{1}{\sqrt{2}}\,r_o + O(\epsilon^2) \qquad (50)$$

and

$$\tilde{\sigma}_{sl}(\Omega) = \frac{\tilde{I}_o}{\sqrt{2}}\,[-2\ln r_o + C_3] + O\left[\frac{1}{Lr_o}, r_o\right] \qquad (51)$$

where the coefficient C_3 is given by

$$C_3 \equiv 2\ln[2^{1/2}\pi] + \int_{-\pi}^{0}\left[\frac{2^{3/2}[\tilde{I}(K_s,\theta) + \tilde{I}(K_s,-\theta)]K_s}{\tilde{I}_o|\tilde{\chi}'_{K_1}|} - \frac{2}{\pi+\theta}\right]d\theta.$$

It is easy to see that the expressions for the inner and outer expansions (43) and (51) contain similar terms $\ln r_o$ which cancel each other when the final sum (31) is calculated. The final expression for the cross section $\tilde{\sigma}_2$ near the frequency $\Omega_h = 2^{1/2}$ is given by (17) with the functions $\tilde{\sigma}_f$ and $\tilde{\sigma}_{sl}$ defined by (18) and (19) [the latter formulas, given in the main text, slightly differ from (43) and (51) by the absence of $\ln r_o$ terms].

Appendix B
Corner Reflection Peak

1) First Simplification of the Integral: We recall that $\tilde{\Gamma}_{\mathrm{EM}}$, the EM component of the nondimensional coupling coefficient $\tilde{\Gamma}$ in the cross-section formula (10), has a sharp peak situated at the circle of radius $R^{1/2} = 1/2$ (see Fig. 5), which leads to the corner reflection peaks in the cross section near the frequency $\Omega_{\mathrm{cr}} = 2^{3/4}$. In the polar coordinates (R,ψ), $\tilde{\Gamma}_{\mathrm{EM}}$ takes the form

$$\tilde{\Gamma}_{\mathrm{EM}} = \frac{-\frac{1}{4} - R\sin^2\psi + 2R}{\sqrt{1-4R} - \tilde{\Delta}_w}.$$

The Cartesian coordinates $(\tilde{p},\tilde{q})$ are expressed in terms of (R,ψ) as follows:

$$\tilde{p} = R^{1/2}\sin\psi \quad \tilde{q} = R^{1/2}\cos\psi$$

where $\tilde{\Delta}_w$ is the nondimensional dielectric impedance of the sea surface discussed in Section II-A. We recall that since $\tilde{\Delta}_w$ is very small, it produces a peak of height $|\tilde{\Delta}_w|^{-2} \gg 1$ and width $|\tilde{\Delta}_w|^2 \ll 1$ in $|\tilde{\Gamma}_{\mathrm{EM}}|^2$ sketched in the upper right insert in Fig. 5.

We rewrite (10) in the polar coordinates (R,ψ)

$$\tilde{\sigma}_2(\Omega) = \frac{L}{2}\int_0^{\infty}\int_{-\pi}^{\pi}\hat{I}(R,\psi)\frac{\sin^2[\pi L(\tilde{\chi}-1)]}{[\pi L(\tilde{\chi}-1)]^2}\frac{dR\,d\psi}{|\sqrt{1-4R}-\tilde{\Delta}_w|^2} \qquad (52)$$

where

$$\hat{I}(R,\psi) \equiv |\sqrt{1-4R} - \tilde{\Delta}_w|^2 \cdot \tilde{I}(K_1(R,\psi),\theta(R,\psi)) \qquad (53)$$

and

$$\begin{aligned}K_1(R,\psi) &= \left[R - R^{1/2}\sin\psi + \frac{1}{4}\right]\\ \theta(R,\psi) &= \arccos\left[\frac{R^{1/2}\sin\psi - \frac{1}{2}}{K_1(R,\psi)}\right].\end{aligned}$$

Here, $\tilde{I}(K_1,\theta)$ describes the smooth part of the integrand and is taken from (11).

The next step is expanding the argument $\tilde{\chi} - 1$ about the saddle point R_s into the Taylor series

$$\tilde{\chi} - 1 = \sum_{n=1}^{\infty}\left.\frac{\partial^n\tilde{\chi}}{\partial R^n}\right|_{R=R_s}\cdot\frac{[R-R_s]^n}{n!} \qquad (54)$$

where $R_s = R_s(\psi,\Omega)$ is the root of

$$\tilde{\chi}(R_s,\psi,\Omega) = 1.$$

Retaining the first term in (54), we reduce the formula cross section (52) (with the accuracy $O(L^{-1})$) to

$$\tilde{\sigma}_2(\Omega) = L\int_0^{\infty}\int_{-\pi/2}^{\pi/2}\hat{I}(R,\psi)\frac{s[\pi L|\tilde{\chi}'_R|(R-R_s)]}{|\sqrt{1-4R}-\tilde{\Delta}_w|^2}dR\,d\psi + O\left[\frac{1}{L}\right] \qquad (55)$$

where $\tilde{\chi}'_R(\psi,\Omega) = (\partial\tilde{\chi}/\partial R)|_{R=R_s(\psi,\Omega)}$. Here, making use of the symmetry of the integrand with respect to the rotation of the angle ψ by π, we changed the integration limits with respect to ψ from $(-\pi,\pi)$ to $(-\pi/2,\pi/2)$ and multiplied the result by the factor of two.

Now, let us consider the integral, first outside the circle $R_o = 1/4$, where we introduce a new coordinate X

$$X = \left[\pi L|\tilde{\chi}'_R|\left(R - \frac{1}{4}\right)\right]^{1/2}, \qquad \left(R > \frac{1}{4}\right)$$

and inside the circle, where we introduce a new coordinate Y

$$Y = \left[\pi L|\tilde{\chi}'_R|\left(\frac{1}{4} - R\right)\right]^{1/2}, \qquad \left(R < \frac{1}{4}\right).$$

We use the fact that $|\tilde{\chi}'_R| = 1$. Then

$$\tilde{\sigma}_2(\Omega) = \frac{L}{2}\int_0^1 \int_{-\pi/2}^{\pi/2} \hat{I}(R[Y],\psi)\frac{s[Z-Y^2]}{(Y-\alpha)^2+\beta^2}\, Y dY d\psi + \frac{L}{2}\int_0^\infty \int_{-\pi/2}^{\pi/2} \hat{I}(R[X],\psi)\frac{s[Z+X^2]}{(X+\beta)^2+\alpha^2}\, X dX d\psi + O\left[\frac{1}{L}\right] \tag{56}$$

where

$$Z = \pi L\left(\frac{1}{4} - R_s(\psi,\Omega)\right)$$
$$\alpha = \frac{(\pi L)^{1/2}}{2}\,\mathrm{Re}(\tilde{\Delta}_w) > 0$$
$$\beta = -\frac{(\pi L)^{1/2}}{2}\,\mathrm{Im}(\tilde{\Delta}_w) > 0.$$

It is easy to see that in (56) there is a large parameter $L \gg 1$ (inside Z) and small parameters $\alpha \sim \beta \ll 1$, which we use for further simplifications. For example, for $L = 100$ and $\tilde{\Delta}_w = 0.011 - i\,0.012$, we have $\alpha \simeq \beta = 0.074$. In terms of these variables, the integrand $\hat{I}(X,\psi)$ is a slow function of its arguments X and ψ: $\partial_X \sim \beta \ll 1$ and $\partial_\psi \sim L^{-1/2} \ll 1$ (the latter will be shown later). Similar behavior holds for $\hat{I}(Y,\psi)$. The integrands $\hat{I}(X,\psi)$ and $\hat{I}(Y,\psi)$ should be expanded into series at the corner reflection region $(X,\psi) = (0,0)$ inside the circle and $(Y,\psi) = (0,0)$ outside the circle. Parameter β specifies the bounds of the region across the circle $R_o = 1/4$ and determines the accuracy ($O(\beta)$) of the asymptotic estimate

$$\tilde{\sigma}_2(\Omega) = \hat{I}_{\mathrm{cr}}\frac{L|\tilde{\Delta}_w|^2}{2}\int_0^\infty \int_{-\pi/2}^{\pi/2} \frac{s[Z-Y^2]}{(Y-\alpha)^2+\beta^2}\, Y dY d\psi + \hat{I}_{\mathrm{cr}}\frac{L|\tilde{\Delta}_w|^2}{2}\int_0^\infty \int_{-\pi/2}^{\pi/2} \frac{s[Z+X^2]}{(X+\beta)^2+\alpha^2}\, X dX d\psi + O\left[\frac{1}{L},\beta\right] \tag{57}$$

where $\hat{I}_{\mathrm{cr}} = \tilde{I}(2^{-1/2}, 3\pi/4)$ is given by (11).

First, we will consider the integration over X and Y and obtain the solution in the form of power series in β and, then, perform the integration over the angle variable ψ.

2) Integration Over Radius: Let us consider the integral

$$J = \int_0^\infty \frac{s[Z+X^2]}{(X+\beta)^2+\alpha^2}\, X dX + \int_0^\infty \frac{s[Z-Y^2]}{(Y-\alpha)^2+\beta^2}\, Y dY. \tag{58}$$

Using the relations

$$\frac{X}{(X+\beta)^2+\alpha^2} = \frac{A}{X+(\beta+i\alpha)} + \frac{A^*}{X+(\beta+i\alpha)^*}$$
$$\frac{Y}{(Y-\alpha)^2+\beta^2} = \frac{B}{Y+i(\beta+i\alpha)} + \frac{B^*}{Y-i(\beta+i\alpha)^*}$$

where "$*$" denotes the complex conjugate and

$$A = \frac{1}{2}\left(1 - i\frac{\beta}{\alpha}\right) \quad B = \frac{1}{2}\left(1 + i\frac{\alpha}{\beta}\right)$$

integral J can be expressed as the sum of four integrals

$$J = J_1 + J_1^* + J_3 + J_3^*$$

where

$$J_1 = A\int_0^\infty \frac{s[Z+X^2]}{X+(\beta+i\alpha)}\, dX$$
$$J_3 = B\int_0^\infty \frac{s[Z-Y^2]}{Y+i(\beta+i\alpha)} dY.$$

Now, consider the first integral J_1 in a slightly different form

$$J_1 = A\int_0^\infty \frac{s[Z+X^2]}{X+\left(1+\frac{i\,\alpha}{\beta}\right)\beta} dX$$

where, recall that $\beta = -((\pi L)^{1/2}/2)\,\mathrm{Im}(\tilde{\Delta}_w) \ll 1$ is a small parameter. One more change of variables $X = t-(1+i\,\alpha/\beta)\,\beta$ in integral J_1 results in

$$J_1 = A\int_{c_1}^\infty \frac{s[Z+t^2]}{t} f(c_1;Z;t)dt$$

where

$$c_1 = \left(1 + \frac{i\,\alpha}{\beta}\right)\beta$$

and

$$f(c_i;Z;t) \equiv e^{-\left[2Zc_i^2+c_i^4+4c_i(c_i^2-Z)t+6c_i^2t^2-4c_it^3\right]}. \tag{59}$$

Similarly, by employing change of variables $Y = t - i(1 + i\,\alpha/\beta)\beta$ in integral J_3, we get

$$J_3 = Be^{-Z^2}\int_{c_3}^\infty \frac{s[Z-t^2]}{t} f(c_3;-Z;t)dt$$

where $c_3 = i(1+i\,\alpha/\beta)\,\beta$. Since $|\beta| \ll 1$, function $f(c_i;Z;t)$ can be expanded in c_i, then, integrals J_1 and J_3 can be presented as a series in c_i

$$J_1 = A\sum_{k=0}^\infty c_1^k \int_{c_1}^\infty b_k(Z,t)\frac{s[t^2+Z]}{t}\, dt \tag{60}$$
$$J_3 = B\sum_{k=0}^\infty c_3^k \int_{c_3}^\infty b_k(-Z,t)\frac{s[t^2-Z]}{t}\, dt \tag{61}$$

where

$$b_k(Z,t) = \frac{1}{k!}\left.\frac{\partial f(c_i;Z;t)}{\partial c_i}\right|_{c_i=0}.$$

3) The Leading Order in β : Here, we will estimate the integral to the leading $O(1)$ order in β. We will not present the second $O(\beta)$ and the third $O(\beta^2)$ order terms of the expansion, because the full details of the calculations and solutions are too lengthy to be presented even in Appendices. Moreover, we found that the leading order solution happened to agree with the numerics with high accuracy. The assumption $\alpha \simeq \beta$ dramatically reduces the calculations without a noticeable lost of accuracy. Although this assumption holds for the range of salinity typical of seawater, it is often not adequate for estuaries and fresh water basins. The compromise we have chosen is as follows: Only in this section, we will give the results without employing this assumption; in the next one, we will presume $\alpha \simeq \beta$.

Let us consider the first item in the sum (60)

$$J_1^{(0)} = A\int_{c_1}^{\infty} \frac{s[t^2+Z]}{t}\,dt = \frac{A}{2}\int_{c_1^2}^{\infty} \frac{s[\tau+Z]}{\tau}\,d\tau.$$

Applying a formal Taylor expansion in Z to the last integral, we find

$$\begin{aligned}\int_{c_1^2}^{\infty} \frac{s[\tau+Z]}{\tau}\,d\tau &= \sum_{n=0}^{\infty}\frac{Z^n}{n!}\int_{c_1^2}^{\infty}\left[\frac{\partial^n}{\partial Z^n}s[\tau+Z]\right]\Bigg|_{Z=0}\frac{d\tau}{\tau}\\ &= \sum_{n=0}^{\infty}\frac{Z^n}{n!}\int_{c_1^2}^{\infty}\frac{\partial^n s[\tau]}{\partial\tau^n}\frac{d\tau}{\tau}\\ &= 2\sum_{n=0}^{\infty}\frac{Z^n}{n!}\int_{c_1^2}^{\infty}\left[\frac{\partial^n}{\partial\tau^n}\sum_{k=0}^{\infty}\frac{(-4)^k\tau^{2k}}{(2k+2)!}\right]\frac{d\tau}{\tau}.\end{aligned} \tag{62}$$

We denote the coefficients at $Z^n/n!$ as μ_n and consider the even powers $n = 2m$

$$\begin{aligned}\mu_{2m} &= 2\int_{c_1^2}^{\infty}\left[\frac{\partial^{2m}}{\partial\tau^{2m}}\sum_{k=0}^{\infty}\frac{(-4)^k\tau^{2k}}{(2k+2)!}\right]\cdot\frac{d\tau}{\tau}\\ &= 2\sum_{k=0}^{\infty}\int_{c_1^2}^{\infty}\frac{(-4)^{k+m}\tau^{2k-1}}{(2k)!(2k+2m+1)(2k+2m+2)}d\tau\\ &= -\frac{(-4)^m[\ln(2c_1^2)+\gamma]}{(2m+1)(m+1)}+\left[\frac{2(-4)^m}{(2m+1)^2}-\frac{2(-4)^m}{(2m+2)^2}\right]\\ &\quad + O(c_1^4)\end{aligned} \tag{63}$$

where $\gamma \simeq 0.57729$ is the Euler constant. The summation over m in (62) results in

$$\sum_{m=0}^{\infty}\frac{\mu_{2m}Z^{2m}}{(2m)!} = -[\ln(2c_1^2)+\gamma]\frac{\sin^2(Z)}{Z^2} + F(Z) \tag{64}$$

where the function $F(Z)$ is

$$F(Z) \equiv \frac{Si(2Z)}{Z} - \frac{Ci(2Z)-\ln(2Z)-\gamma}{2Z^2} - \frac{\sin^2(Z)}{Z^2} \tag{65}$$

and $Si(x)$ and $Ci(x)$ are the integral sine and cosine functions (see, e.g., [15]).

There is no necessity to consider the odd coefficients μ_{2m+1} since in the sum the corresponding contributions from $J_1^{(0)}$ will be cancelled by their counterparts in integral $J_3^{(0)}$ containing $(-Z)^{2m+1}$. Then, to the zeroth order, integral J is

$$\begin{aligned}J^{(0)} &= 2\mathrm{Re}\left[J_1^{(0)}+J_3^{(0)}\right]\\ &= \mathrm{Re}\left[A\int_{c_1^2}^{\infty}\frac{s[\tau+Z]}{\tau}\,d\tau + B\int_{c_3^2}^{\infty}\frac{s[\tau-Z]}{\tau}\,d\tau\right] =\\ &= \mathrm{Re}\left[(A+B)\sum_{m=0}^{\infty}\frac{\mu_{2m}Z^{2m}}{(2m)!}+(A-B)\sum_{m=0}^{\infty}\frac{\mu_{2m+1}Z^{2m+1}}{(2m+1)}\right]\\ &= d_0\,s(Z)+F(Z)+O(\beta^4)\end{aligned} \tag{66}$$

where d_0 in the generic case (i.e., $\alpha \neq \beta$) is

$$d_0 = -2\ln|\beta| - \ln\left[1+\frac{\alpha^2}{\beta^2}\right] - \left[\frac{\beta}{\alpha}-\frac{\alpha}{\beta}\right]\arctan\frac{\alpha}{\beta}+\frac{\alpha}{\beta}\frac{\pi}{2}-\frac{\gamma}{2}. \tag{67}$$

4) Integration Over Angle: Although the calculations were also performed up to the third order in β, it proved to be sufficient in evaluating $\tilde{\sigma}_2(\Omega)$ for purposes of this paper to confine analysis to the leading order in β only

$$\tilde{\sigma}_2(\Omega) = \hat{I}_{\mathrm{cr}}\frac{L|\tilde{\Delta}_w|^2}{2}\int_{-\pi/2}^{\pi/2}(d_0 s[Z(\psi)]+F[Z(\psi)])\,d\psi + O\left[\frac{1}{L},\beta\right] \tag{68}$$

where

$$Z(\psi) = \pi L\left[\frac{1}{4} - R_s(\psi,\Omega)\right]$$

and d_0 from (67) was simplified using $\alpha \approx \beta$ to

$$d_0 = -2\ln c - 2\ln 2 - \gamma + \frac{\pi}{2}.$$

The next step is integration over ψ. The variable Z can be represented in the form

$$Z = \zeta + \tilde{\xi}^2$$

where

$$\zeta \equiv \pi L\left[\frac{1}{4} - R_s(0,\Omega)\right] = \pi L\frac{\Omega^4-8}{2\Omega^4}$$

$$\tilde{\xi}^2 \equiv \pi L\chi''_{\psi\psi}\frac{\psi^2}{2} = \frac{3\pi}{16}L\psi^2.$$

Let us analyze the first term in (68). Let us treat separately the part that does not depend on $\xi_l = \tilde{\xi}_l^2 = (3\pi^3/64)L$, and the part that does depend on ξ_l

$$\begin{aligned}&\int_{-\pi/2}^{\pi/2} s[Z(\psi)]d\psi\\ &\quad= \left(\frac{16}{3\pi L}\right)^{1/2}\int_{-\tilde{\xi}_l}^{\tilde{\xi}_l} s[\zeta+\tilde{\xi}^2]d\tilde{\xi}\\ &\quad= 2\left(\frac{16}{3\pi L}\right)^{1/2}\left[\int_0^{\infty} s[\zeta+\tilde{\xi}^2]d\tilde{\xi} - \int_{\tilde{\xi}_l}^{\infty} s[\zeta+\tilde{\xi}^2]d\tilde{\xi}\right]\\ &\quad= \left(\frac{16}{3\pi L}\right)^{1/2}\left[\int_0^{\infty} s[\zeta+\xi]\frac{d\xi}{\xi^{1/2}} - \int_{\xi_l}^{\infty} s[\zeta+\xi]\frac{d\xi}{\xi^{1/2}}\right].\end{aligned} \tag{69}$$

We denote the first integral in (69) as $Sj(\zeta)$

$$Sj(\zeta) \equiv \int_0^{\infty} s[\zeta+\xi]\frac{d\xi}{\xi^{1/2}} = \sum_{n=0}^{\infty}\frac{\zeta^n}{n!}\int_0^{\infty}\frac{\partial^n s[\xi]}{\partial\xi^n}\frac{d\xi}{\xi^{1/2}}. \tag{70}$$

Performing integration over ξ and summation in (70) similarly to that just described in Appendix B3, we can express function $Sj(\zeta)$ in a tractable closed form

$$\begin{aligned}Sj(\zeta) &= \pi\zeta^{-3/2}\left(\frac{1}{4}+\zeta\right)F_C\left[\left(\frac{4\zeta}{\pi}\right)^{1/2}\right] - \frac{\pi^{1/2}}{2\zeta}\cos(2\zeta)\\ &\quad + \pi\zeta^{-3/2}\left(\frac{1}{4}-\zeta\right)F_S\left[\left(\frac{4\zeta}{\pi}\right)^{1/2}\right] - \frac{\pi^{1/2}}{2\zeta}\sin(2\zeta)\end{aligned} \tag{71}$$

where F_C and F_S are the Fresnel cosine and sine integrals [15].

The second integral in (69) can be estimated using the assumption $|\zeta| < \xi_l/2$

$$\int_{\xi_l}^{\infty} s[\zeta+\xi]\frac{d\xi}{\xi^{1/2}} < \int_{\xi_l}^{\infty}\frac{d\xi}{(\zeta+\xi)^2\xi^{1/2}} < 4\int_{\xi_l}^{\infty}\frac{d\xi}{\xi^{5/2}} = O\left[\frac{1}{L^{3/2}}\right].$$

Hence

$$\int_{-\pi/2}^{\pi/2} s[Z(\psi)]d\psi = \left(\frac{16}{3\pi L}\right)^{1/2} Sj(\zeta) - O\left[\frac{1}{L^2}\right]. \qquad (72)$$

The integral with $F[Z(\psi)]$ in (68) can be treated similarly

$$\int_{-\pi/2}^{\pi/2} F[Z(\psi)]d\psi = \left(\frac{16}{3\pi L}\right)^{1/2} Fj(\zeta) - O\left[\frac{1}{L^2}\right] \qquad (73)$$

where $Fj(\zeta)$ is defined as

$$Fj(\zeta) \equiv \int_{-\infty}^{\infty} F[\zeta+\tilde{\xi}^2]d\tilde{\xi} = \sum_{n=0}^{\infty}\frac{\zeta^n}{n!}\int_0^{\infty}\frac{\partial^n F[\xi]}{\partial \xi^n}\frac{d\xi}{\xi^{1/2}}. \qquad (74)$$

Fj can be presented as (75), shown at the bottom of the page, where ${}_2F_3$ are the generalized hypergeometric functions described in Appendix C.

Thus, near the corner-reflection frequency $\Omega_{\mathrm{cr}} = 2^{3/4}$, the second-order cross section $\tilde{\sigma}_2(\Omega)$ can be approximately presented as

$$\tilde{\sigma}_2(\Omega) = \hat{I}_{\mathrm{cr}}\left|\frac{4L\tilde{\Delta}_w^4}{3\pi}\right|^{1/2}\{d_0\, Sj(\zeta) + Fj(\zeta)\} + O\left[\beta, \frac{1}{L}\right]. \qquad (76)$$

Appendix C
Generalized Hypergeometric Functions

We use the generalized hypergeometric functions ${}_2F_3$ given in notations by Prudnukov [16] (their definition is similar to that for the usual hypergeometric functions given in a well-known handbook [15])

$$ {}_2F_3\left[\begin{matrix} a_1, a_2 \\ b_1, b_2, b_3\end{matrix}; z\right] \equiv {}_2F_3\left[a_1, a_2; b_1, b_2, b_3; z\right] = \sum_{k=0}^{\infty}\frac{(a_1)_k\,(a_2)_k}{(b_1)_k\,(b_2)_k\,(b_3)_k\; k!}\, z^k \qquad (77)$$

where

$$(a_n)_k \equiv \frac{\Gamma[a_n+k]}{\Gamma[a_n]}.$$

The generalized hypergeometric function ${}_2F_3[1/2, 1/2; 3/2, 3/2, 2; -x^2]$ used in Appendices A and B have a logarithmic asymptotics at large values of the argument

$${}_2F_3\left[\frac{1}{2}, \frac{1}{2}; \frac{3}{2}, \frac{3}{2}, 2; -x^2\right] = \frac{\ln x + C_1}{x} + O\left[\frac{1}{x^3}\right]. \qquad (78)$$

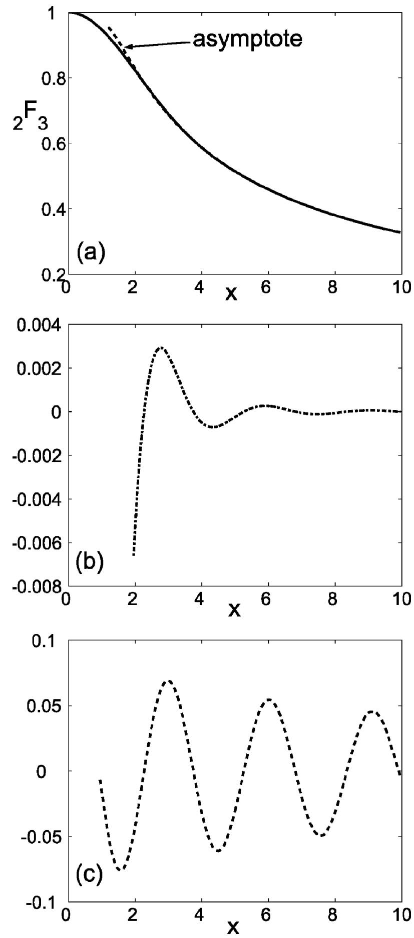

Fig. 10. (a) Function ${}_2F_3[1/2, 1/2; 3/2, 3/2, 2; -x^2]$ (solid) and its asymptote $(\ln x + C_1)/x$ (dashed), $C_1 = 0.96351$. (b) Discrepancy ${}_2F_3[1/2, 1/2; 3/2, 3/2, 2; -x^2] - (\ln x + C_1)/x$. (c) Verification of the behavior of the residual term $x^3({}_2F_3[1/2, 1/2; 3/2, 3/2, 2; -x^2] - (\ln x + C_1)/x)$.

Here, the constant C_1 could be derived analytically in terms of the Gamma functions, we, however, took the easier way and estimated the constant numerically. We found that $C_1 \approx 0.96351$ and the corresponding results are presented in Fig. 10. Function ${}_2F_3[1/2, 1/2; 3/2, 3/2, 2; -x^2]$ and its asymptote $(\ln x + C_1)/x$ are shown in Fig. 10(a). The discrepancy between the function and its asymptote ${}_2F_3[1/2, 1/2; 3/2, 3/2, 2; -x^2] - (\ln x + C_1)/x$ is shown in Fig. 10(b). Finally, the correctness of the term $O[1/x^3]$ is checked in Fig. 10(c), where function $x^3\left({}_2F_3[1/2, 1/2; 3/2, 3/2, 2; -x^2] - (\ln x + C_1)/x\right)$ is plotted. Thus, there is nearly perfect representation of the function by its asymptotic approximation given by (78).

$$Fj(\zeta) = \pi^{1/2}\left\{4\,{}_2F_3\left[\begin{matrix}\frac{1}{4}, \frac{1}{4} \\ \frac{1}{2}, \frac{5}{4}, \frac{5}{4}\end{matrix}; -\zeta^2\right] - \frac{4}{9}\,{}_2F_3\left[\begin{matrix}\frac{3}{4}, \frac{3}{4} \\ \frac{1}{2}, \frac{7}{4}, \frac{7}{4}\end{matrix}; -\zeta^2\right]\right\} + \pi^{1/2}\zeta\left\{\frac{8}{25}\,{}_2F_3\left[\begin{matrix}\frac{5}{4}, \frac{5}{4} \\ \frac{3}{2}, \frac{9}{4}, \frac{9}{4}\end{matrix}; -\zeta^2\right] - \frac{8}{9}\,{}_2F_3\left[\begin{matrix}\frac{3}{4}, \frac{3}{4} \\ \frac{3}{2}, \frac{7}{4}, \frac{7}{4}\end{matrix}; -\zeta^2\right]\right\} \qquad (75)$$

ACKNOWLEDGMENT

The authors would like to thank A. Y. Orlov for his crucial input concerned with derivation of asymptotics of the generalized hypergeometric functions without which this work would not have reached the present completeness.

REFERENCES

[1] P. Broche *et al.*, "VHF radar for ocean surface current and sea state remote sensing," *Radio Sci.*, vol. 22, no. 1, pp. 69–75, 1987.
[2] J. D. Paduan and H. Graber, "Introduction to high-frequency radar: Reality and myth," *Oceanogr.*, vol. 10, no. 2, pp. 36–39, 1997.
[3] L. R. Wyatt, "Limits to the inversion of HF radar backscatter for ocean wave measurement," *J. Athmos. Ocean. Technol.*, vol. 17, no. 12, pp. 1651–1665, 2000.
[4] D. D. Crombie, "Doppler spectrum of sea echo at 13.56 mc/s," *Nature*, vol. 175, pp. 681–682, 1955.
[5] B. L. Weber and D. E. Barrick, "On the nonlinear theory for gravity waves on the ocean's surface. Part I: Derivations," *J. Phys. Oceanogr.*, vol. 7, no. 1, pp. 3–10, 1972.
[6] ——, "On the nonlinear theory for gravity waves on the ocean's surface. Part II: Interpretation and applications," *J. Phys. Oceanogr.*, vol. 7, no. 1, pp. 11–21, 1972.
[7] B. J. Lipa and D. E. Barrick, "Extraction of sea state from HF radar sea echo: Mathematical theory and modeling," *Radio Sci.*, vol. 21, no. 1, pp. 81–100, 1986.
[8] D. E. Barrick, M. W. Evans, and B. L. Weber, "Ocean surface currents mapped by radar," *Science*, vol. 198, pp. 138–144, 1977.
[9] D. E. Barrick, "Theory of HF anf VHF propagation across the rough sea. The effective surface impedance for a slightly rough highly conducting medium at grazing incidence radar," *Radio Sci.*, vol. 6, pp. 517–526, 1971.
[10] J. Walsh and E. W. Gill, "An analysis of the scattering of high-frequency electromagnetic radiation from rough surfaces with application to pulse radar operating in backscatter mode," *Radio Sci.*, vol. 35, no. 6, pp. 1337–1359, 2000.
[11] V. I. Shrira, D. V. Ivonin, P. Broche, and J. C. de Maistre, "On remote sensing of vertical shear of ocean surface currents by means of a single-frequency VHF radar," *Geophys. Res. Lett.*, vol. 28, no. 20, pp. 3955–3958, 2001.
[12] D. V. Ivonin, P. Broche, J.-L. Devenon, and V. Shrira, "Validation of HF radar probing of the vertical shear of surface currents by ADCP measurements," *J. Geophys. Res.*, vol. 109, no. C4, pp. 1–8, Apr. 2004.
[13] O. M. Phillips, *The Dynamics of the Upper Ocean*. Cambridge, U.K.: Cambridge Univ. Press, 1966.
[14] F. W. Olver, *Asymptotics and Special Functions (Computer Science and Applied Mathematics)*. New York: Academic, 1974.
[15] M. Abramowitz and I. Stegun, *Handbook of Matematical Functions*, 9th ed. New York: Dover, 1974.
[16] A. P. Prudnikov, Y. A. Brychkov, and O. I. Marichev, *Integrals and Series*. Boca Raton, FL: CRC, 1990, vol. 3, More Special Functions.

Dmitry V. Ivonin received the M.S. degree in applied physics and mathematics from the Moscow Institute of Physics and Technology, Moscow, Russia, in 1995 and the Ph.D. degree in physical oceanography from the Shirshov Institute for Oceanology, Russian Academy of Sciences (RAS), Moscow, Russia, in 2001.

Since 1995, he has been an Engineer in the Laboratory of Nonlinear Wave Process, Shirshov Institute for Oceanology, RAS. His research interests include wave current interactions, HF radio oceanography, and laminar-turbulent transition in the free-surface boundary layers.

Victor I. Shrira received the M.S. degree in radiophysics from the Nizhny Novgorod State University, Nizhny Novgorod, Russia, in 1975 and the Ph.D. degree in physical oceanography from the Shirshov Institute for Oceanology, Russian Academy of Sciences (RAS), Moscow, Russia, in 1981.

From 1980 to 1997, he has been a Scientist, Senior and Leading Scientist, and Head of Wave-Current Interaction Group at the Shirshov Institute for Oceanology, RAS. In 1977, he was appointed *The Benson Ford Professor in Applied Mathematics* at University College Cork, Cork, Ireland, where he worked till 2000, at the same time keeping his position at the Shirshov Institute. Since 2000, he has been a Professor in Applied Mathematics at Keele University, Keele, U.K. Since 1994, he has been an Editor of *Nonlinear Processes in Geophysics*. His research is in the general theory of nonlinear waves, basic fluid dynamics, waves in the ocean (primarily wind waves, internal and Rossby waves, and vorticity waves), wave current interactions, EM scattering from the sea surface, and HF radar oceanography.

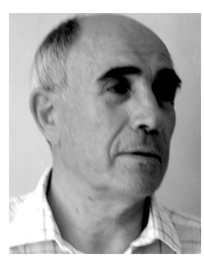

Pierre Broche received the M.S. degree in physics from École Normale Supérieure, Paris, France, in 1965 and the Ph.D. degree from Faculté des Sciences de Paris, Université Paris, Paris, France, in 1969.

He is currently a Professor at the Université de Toulon et du Var, La Garde, France. He has over 30 years experience in radar remote sensing of the sea surface and its application for coastal studies (wind waves and currents, river plumes, etc.).